Fluidic Jet Barriers for the Reduction of Leakage Loss in Shrouded Turbines

GEET NAUTIYAL

Fluidic Jet Barriers for the Reduction of Leakage Loss in Shrouded Turbines

Geet Nautiyal

Tip leakage flows are a significant source of performance reduction in shrouded turbines. In this study, the leakage loss was addressed using the concept of fluidic jet barriers. The fluidic jet was employed:

- To form a seal so that less flow entered the leakage channel and passed through the blade passage instead.
- To impart a tangential momentum to the leakage flow and turn it towards the direction of the blade exit bulk flow.

This potential was explored using three dimensional steady state RANS CFD simulations that were first validated against experimental data. A commercial test campaign conducted on a leakage flow analysis cascade at Durham provided the data. The cascade data was then compared with its corresponding CFD analysis. Five turbulence models were tested and the model that matched the experiment most closely was selected. Then the fluidic jet was implemented on a best practice design of a shrouded rotor used in the industry. For this, first a baseline case was designed using the Durham Cascade as reference. Then it was modified to incorporate the fluidic jet. Four fluidic jet configurations were tested and the best performing configuration was selected. The jet pressure was gradually increased up to the overblown condition, i.e., when a part of the jet fluid turned upstream and entered through the inlet cavity.

As predicted, the fluidic jet was successful in increasing the blade work and reducing the mixing loss. Furthermore, it also improved the yaw angle distribution at the rotor exit. Therefore, the present study served to show for the first time, that fluidic jets can be used to address bypass effect as well as re-entry mixing loss in shrouded turbines. The favourable impact on the downstream incidence indicated that they also have the potential to reduce the secondary losses in downstream rows.

Fluidic Jet Barriers for the Reduction of Leakage Loss in Shrouded Turbines

Geet Nautiyal

A Thesis presented for the degree of
Master of Science by Research

School of Engineering
University of Durham
England
July 2014

Contents

List of Figures

List of Tables

Nomenclature

	Cp	Pressure Coefficient
	c_p	Specific Heat of Air
	Cp_0	Total Pressure Loss Coefficient
	F	Net Blade/Shroud Force
	$\dot{m}$	Mass Flow Rate
	P	Pressure
	Re	Reynolds Number
	S	Entropy
	T	Static Temperature
	U	Blade Velocity
	V	Air Velocity
	W	Air Velocity Relative to Rotor Blade
	C_x	Blade Axial Chord
	α	Absolute Yaw Angle
	β	Relative Yaw Angle
	γ	Ratio of Specific Heats
	ε	Turbulent Dissipation Rate
	θ	Fluidic Jet Incline Angle
	λ	Thermal Conductivity
	μ	Viscosity
	ϱ	Density
	ϕ	Flow Coefficient
	ψ	Work Coefficient
Subscripts	0	Total
	1	Rotor Inlet

2	Rotor Outlet
eff	Effective
j	Jet Inlet
rel	Relative to Rotor Blade
s	Static
x / y / z	Axial / Tangential /Radial Coordinates

Declaration

The work in this thesis is based on research carried out in the School of Engineering at the University of Durham. No part of this thesis has been submitted elsewhere for any other degree or qualification and it is all my own work unless referenced to the contrary in the text.

Acknowledgements

The author is indebted to the many people who helped him in the successful completion of this thesis. My sincere thanks are due to my supervisor Dr. Grant Ingram for his precious guidance and for his unique way of keeping his students motivated. I am extremely grateful to my second supervisor, Dr. Richard Williams, who not only helped me tremendously in the experimental work, but also gave invaluable advices throughout my MSc project. Furthermore, it is easy to overlook one's mistakes when working on a thesis for too long and no author can deny the importance of a fresh unbiased eye. So, I would like to especially thank him for his several reads of my thesis and for pointing out where I needed to make improvements. Dr. Simon Hogg, also my supervisor, deserves a special mention for the useful discussion on the fluidic jet implementation.

Dr. David Sims-Williams was very kind in helping me with the probe calibration. I would like to express my gratitude towards Michael Hilfer for always taking the time out whenever I needed help or advice on a wide range of issues dealing with both experimental and numerical work. I would also like to thank Andrew Messenger who provided me with the design of the fluidic jet rig in the Thermo Lab, as well as his MEng project report. I am grateful to Colin Wintrip, Paul Jarvis, Stuart Watson and Phillip Duffy in the Mechanical Workshop for their assistance and for lending useful equipment during the cascade work. James Dobson deserves my special thanks for teaching me how to run simulations on the computing cluster Hamilton and for giving me the relevant software.

Delays related to the fulfillment of the various visa conditions are common for international students and my thanks are due to Mrs. Debra Smith in the administration for her support throughout my long admission process. Discussions on turbine aerodynamics with Thomas Frech were also cherished.

1 Introduction

In axial flow turbines, like in any other turbomachinery, there are inevitable gaps between the stationary and rotating parts of the machine. For example, gaps can be found between the rotor blade tip and the casing, the stator blade tip and the hub or the wheel space between the rotor and the stator. Due to the pressure difference across these gaps, a portion of the working fluid leaves the bulk flow and leaks through these gaps. Since the leakage flow bypasses the blades, it reduces the blade work. Moreover, its interaction with the bulk flow creates losses and causes a reduction in the useful energy of the working fluid. So the work that can be extracted by the downstream stages is also reduced. Additionally, this interaction may modify the incidence on the downstream rows, creating further losses. Leakage flows are therefore detrimental to the turbine performance. In fact, tip leakage loss can account for up to one third of the total thermodynamic loss in early turbine stages [1].

Fluidic jets have recently been shown to reduce the tip leakage flow rate in shrouded turbines [2-4]. The present study aimed to expand the domain of fluidic jet application by using it to control the shroud leakage as well as the associated mixing losses. A Computational Fluid Dynamics (CFD) based approach was taken to incorporate a fluidic jet into a generic industrial turbine rotor. Figure 1 shows the rotor and the siting of the fluidic jet.

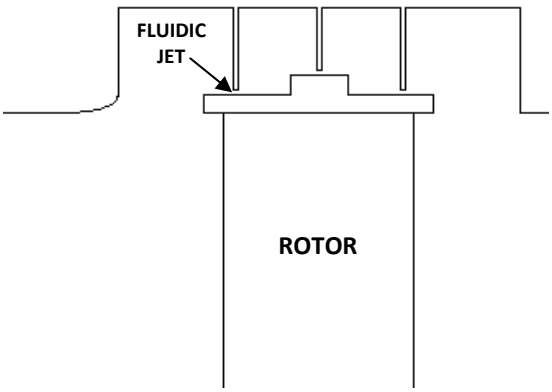

Figure 1, Fluidic Jet Incorporation

The remainder of this thesis is structured as follows:

2. **Literature Review:** This chapter presents an overview of part studies undertaken in the field of turbine shroud leakage flows.

3. **Leakage Loss Reduction:** The rationale behind investigating the application of fluidic jets is described in this chapter.

4. **CFD Validation:** This chapter presents the validation case which is the leakage flow analysis cascade, along with the experimental technique used to take the test data. It then describes the application of the computational methodology to the validation test case. Finally, it shows a comparison of the test data with five different turbulence closure models and then selects the best performing model.

5. **The Baseline Case:** The baseline case of the present study is introduced in this chapter. This is a turbine half-stage without a fluidic jet. Its geometry, mesh, boundary conditions and the main flow features are described.

6. **Fluidic Jet Cases:** The various fluidic jet configurations that were tested in this study are presented in this chapter. A comparative performance analysis is conducted and the procedure for the selection of the final configuration is explained.

7. **Results Analysis:** This chapter describes the flow features of the selected fluidic jet case and compares them with the ones of the baseline case. Then it investigates the fluidic jet impact on the pitch-averaged flow field and loss distribution at the rotor exit. It ends by considering other turbine aspects such as work and flow coefficients and their effect on the fluidic jet performance.

8. **Discussion:** A discussion based on the interpretation of the results is presented.

9. **Conclusions**

10. **Recommendations**

11. **References**

2 Literature Review

Two main types of turbine tip configuration have are in use in the industry: shrouded and unshrouded. At very low values of tip clearance, unshrouded turbines show a higher total-to-total efficiency [5]. This is because, in shrouded turbines, the presence of the cavities causes entropy generation inside them and enhances the secondary flows. However, as the tip clearance is increased, there is a 'break-even clearance' above which shrouded turbines become more efficient than unshrouded ones, its exact value depending on the particular turbine [5]. The reason is that, at higher clearances, the interaction between the tip leakage flow and the bulk flow is much stronger in unshrouded blades [6], resulting in higher mixing loss. Furthermore, the shroud geometry enables the shrouded turbines to use multiple seals which helps to reduce the leakage flow rate [1].

2.1 Shrouded Turbine Flows

The flow through a shrouded turbine splits between the leakage flow that passes over the shroud and the bulk flow that passes through the blade passage.

2.1.1 Leakage Flow

Figure 2 illustrates the tip leakage flow over a shrouded turbine.

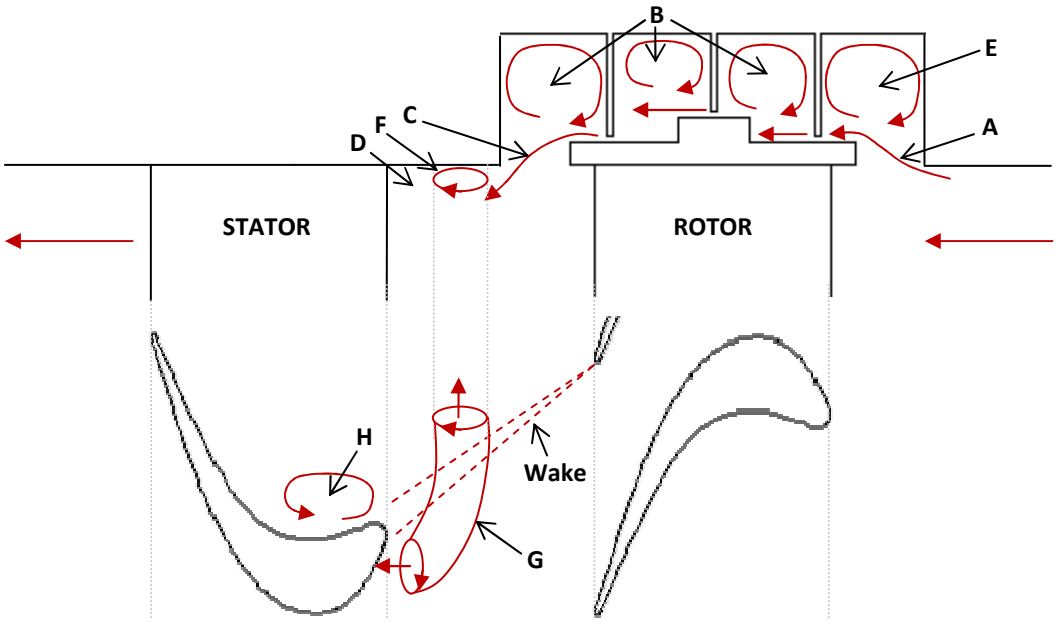

Figure 2, Turbine Shroud Leakage Flow

Axial and radial gaps, between the shroud and the casing, allow for rotor axial and radial movements during the turbine operation. A portion of the bulk flow enters through the upstream axial gap and passes over the shroud (**A**). It is then squeezed through the seal radial clearances forming jets that mix and form vortical structures in the downstream cavity space (**B**). Finally, the leakage flow re-enters the bulk flow through the downstream axial gap and creates further mixing (**C**). The effect of this mixing is seen to be carried through the downstream stator (**D**). The driving force of the leakage flow is the pressure drop across the blade passage (upstream and downstream of the blade).

2.1.2 Bulk Flow

The bulk flow contains features such as secondary flows and wakes. The secondary flow development in turbines, as illustrated by Takeshi et al. [7] in Figure 3, is a complex process.

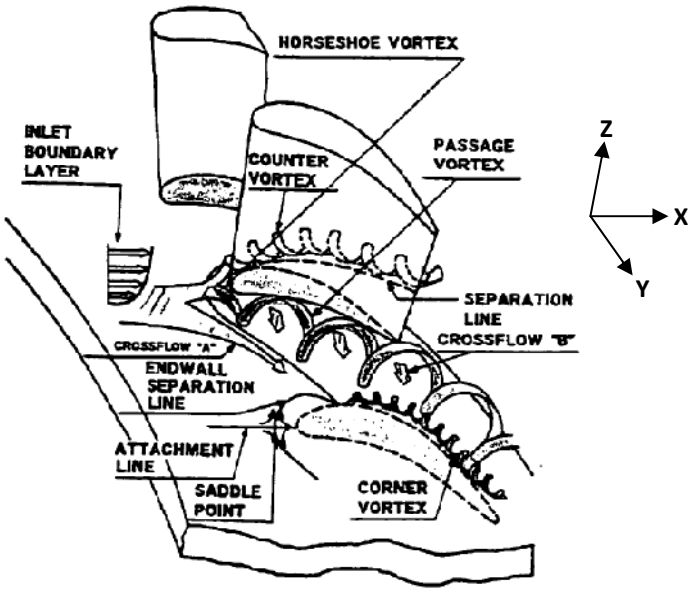

Figure 3, Secondary Flow Model [7]

When the end wall boundary layer passes through the blade passage, the slow moving fluid near the end wall undergoes a higher turning leading to a cross flow. This leads to the formation of the passage vortex which is the largest secondary flow structure. Another notable feature is the horseshoe vortex which is formed due to the rolling-up of the inlet end wall boundary layer when it meets the blade leading edge.

The pressure side leg of the horseshoe vortex has the same sense of rotation as the passage vortex and so has a strong interaction with it. The suction side leg (shown as counter vortex in the figure) also interacts with the passage vortex but rotates in an opposite sense. It is usually seen to climb onto the suction surface towards the mid span. Sometimes an extra feature known as the corner vortex exists in blades with high turning. It is formed on the suction surface – end wall corner, and rotates in the opposite sense to the passage vortex.

Wakes are formed behind the blades as a result of boundary layer development on the blade surface and their separation at the blade trailing edge.

2.2 Shroud Leakage Loss Mechanisms

Due to its complex nature, it is useful to break the shroud leakage process into the different ways in which it impacts the turbine performance: The bypass effect is essentially an inviscid mechanism that reduces the rotor work. Four viscous loss mechanisms, associated with such flows, were identified by Rosic et al. [8]: mixing inside cavities, mixing between the re-entering leakage flow and the bulk flow, the impact on downstream rows and windage due to wall friction. It is important to understand these mechanisms in order to successfully reduce the leakage loss and, thus, improve the turbine efficiency.

2.2.1 Bypass Effect

The leakage flow leaves the bulk flow and passes over the shroud, thus "bypassing" the blade passage. So it does not participate in the work exchange between the fluid and the rotor blades, reducing the work output from the turbine stage.

2.2.2 Mixing Inside Cavities

As the leakage flow passes over the shroud, the leakage jet from each seal gap expands into the cavity space downstream and dissipates its kinetic energy. Furthermore, it forms vortical structures inside the cavities. These mixing phenomena lead to a drop in the total pressure of the cavity fluid and so generate loss.

The inlet cavity fluid may show a high unsteadiness due to its interaction with the bulk flow. Hot wire traverses were conducted by Wolter et al. [9] inside the rotor shroud cavities. These measurements revealed that the inlet cavity featured the most unsteady flow with velocity and flow angle fluctuations of ±5 m/s and ±12 degrees respectively. The reason for the unsteadiness was found to be the influence of the rotor and the upstream stator potential fields. The unsteady behaviour was damped immediately after the first seal tooth with negligible temporal fluctuations in the middle cavity. The unsteadiness re-emerged in the exit cavity due to bulk flow influence, but not to the extent seen in the inlet cavity.

Mixing inside the inlet cavity also enhances the secondary flows within the rotor. The reason for this was revealed by Pfau et al. [10] who performed detailed measurements inside the rotor inlet cavity of a two-stage low speed turbine and noticed a toroidal vortex moving at 90 percent of the rotor blade tip speed (**E** in Figure 2). The vortex was found to be stretched and tilted in space and time due to the interaction of the rotor potential field with that of the upstream stator. This vortex interacted with the bulk flow and caused negative incidence on the rotor enhancing its secondary flows.

2.2.3 Mixing at Re-entry

Denton et al. [11] experimentally showed that the shroud leakage flow maintains its original direction and undergoes little turning compared to the bulk flow through the blade passage. Therefore, the re-entering leakage flow has a different velocity from the bulk flow and this causes intense mixing leading to loss production. Re-entry mixing is a significant component of the shroud leakage loss [12]. Denton [1] worked out a simple analytical model to estimate the entropy rise associated with this mixing. The entropy creation was seen to primarily depend upon the leakage flow rate and the difference in the axial and tangential velocity components of the leakage and the bulk flows.

2.2.4 Downstream Row Impact

Shroud leakage has a significant impact on the downstream blade rows, especially in terms of their secondary flows and hence the secondary loss. The influence of the leakage interaction on the downstream row was investigated in detail by Peters et al. [13] who performed an experimental and numerical study on a 1.5-stage low speed turbine. The leakage interaction caused a negative incidence on the downstream stator near the casing and thus the stagnation point moved towards the suction surface. Due to this, a radial pressure gradient towards the hub was formed on the suction surface and an opposite gradient towards the casing was formed on the pressure surface of the stator blade. Since the flows induced by these pressure gradients were in the same sense as the stator passage vortex, the latter was enhanced. In fact, the stator passage vortex was seen to cover half the area of the turbine annulus. Shroud leakage flows have been shown to modify the inlet flow conditions for up to two rows downstream of the interaction ([14], [15]).

Leakage flow also produces unsteadiness in the downstream rows. The following mechanisms are described in the literature that may account for it:

- There is bulk flow ingress to the exit cavity near the wake pressure side. This breaks the leakage sheet from the last sealing fin into distinct periodic jets, a process that is further enhanced by the passage vortex [16] as shown in Figure 4. It can be inferred that, in a real machine, this phenomenon would result in periodic negative incidences on the downstream blade row, resulting in high unsteadiness.

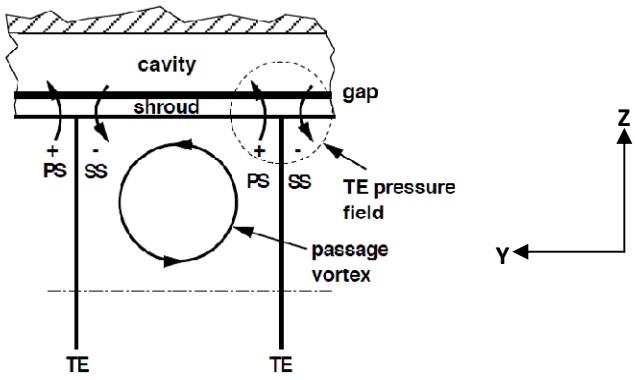

Figure 4, Unsteadiness Driving Mechanisms [16]

- In case of a sharp exit cavity edge, there is flow separation which forms a toroidal vortex behind the rotor on the casing wall (**F** in Figure 2). The axis of this vortex changes direction from almost parallel to the turbine axis on the wake pressure side to perpendicular to it near the suction side [17] (**G** in Figure 2). Owing to this circumferential variation, the downstream stator sees constant incidence conditions for only a fraction of the rotor blade passing period. A large recirculation zone may be observed on the stator pressure side for the rest of the period [17] (**H** in Figure 2).

As an evidence of this unsteadiness, Giboni et al. [18] in their time-accurate measurements on a 1.5-stage low speed turbine observed fluctuations of ±20 percent in the velocity and 30 to 90 degrees in the yaw angle at the rotor exit near the casing region. This was detrimental to the performance of the downstream stator which, in addition to generating a large passage vortex, showed fluctuations of up to 3 degrees in its exit yaw angle. Another impact of this unsteadiness was demonstrated in the time-accurate measurements and unsteady computations by Peters et al. [19]. They showed that the secondary flow development in the downstream stator varied significantly with the relative position of the upstream rotor. When the leakage jet directly entered the stator passage, it enhanced the end wall crossflow (seen in Figure 3). So, there was a high overturning near the casing with no well-defined centre of the passage vortex. At other times, the passage vortex developed more distinctly, but these differences reduced towards the stator exit. Time-resolved blade static pressure profiles by Adami et al. [14] also showed higher fluctuations near the leakage – bulk flow interaction region, confirming its unsteady nature.

2.2.5 Windage

Windage loss is generated due to the viscous friction between the cavity fluid and the shroud/casing/hub wall. As it is quite negligible compared to the other loss generation mechanisms, it has generally been neglected in the analyses of leakage flows. Gier et al. [12] quantified the windage loss contribution in their simulation of a three-stage LP turbine for jet engines and found it to be 2.5 percent of the total loss.

Windage loss can be reduced by minimizing the shroud/casing/hub surfaces that are exposed to the cavity fluid.

2.3 CFD Considerations

2.3.1 The Importance of Cavity Modeling

It can be understood from these loss mechanisms that the leakage process in shrouded turbines is quite complex and is three-dimensional in nature. So, while performing CFD simulations of shrouded turbines, it is essential to model the cavities fully in order to obtain a reasonable prediction of the flow features and their effect on performance. This was shown by Rosic et al. [20] who compared their experiments on a three-stage low speed turbine with three simulations: first without leakage, second with a simple leakage model of sources and sinks at the end walls and the third with all leakage paths and cavities computed. Only the third simulation was able to match the experimental trends and flow features correctly, especially in the later turbine stages. Similar findings were reported by Cherry et al. [21] who worked on the low pressure turbine stages of a high bypass turbofan engine.

When the flow inside the cavities was investigated by [20], it was found to be very complex and this was the reason for the lower fidelity of the simple models. For example, the interaction between the cavity fluid and the bulk flow was not uniform in the pitch-wise direction. The bulk flow was seen to be pushed more into the inlet cavity near the blade leading edge, leading to its non – uniform entry into the first seal. At the exit cavity, there was a net inflow near the wake pressure side which changed to a net outflow towards the wake suction side. This pitch-wise non-uniformity has also been observed by other authors (e.g. [8], [22]).

Hence, all shroud cavities were fully modeled in the present CFD simulations.

2.3.2 Computational Strategy

The unsteady effects observed in the literature reviewed in section 2.2 suggest that time-accurate computations are required when simulating turbine shroud leakage flows. However, steady simulations have been found to be adequate for capturing

the average leakage flow effects [23]. Moreover, steady flow simulations give substantial benefits in terms of the computational time and effort required. Above all, the primary focus of the present study was to investigate the potential of fluidic jets in reducing the leakage loss at the rotor exit. So, steady state CFD on a single rotor configuration was considered sufficient for the work presented in this thesis.

2.4 Leakage Loss Reduction Techniques

2.4.1 Seal Design

A major factor which determines the fraction of the fluid leaving the bulk flow is the clearance between the seal teeth and the casing/hub wall. So it is important to minimize the seal clearances in order to increase the turbine performance. This was shown by Rosic et al. [8] who performed clearance variation in their numerical simulations of a three-stage low speed turbine As the clearances were increased, the rotor secondary flows were reduced due to an increased removal of the incoming boundary layer. However its beneficial effect was cancelled by the enhancement of the downstream stator secondary flows, so that, ultimately, there was a drop in the turbine efficiency. This efficiency drop was proportional to the leakage mass fraction.

A minimum clearance is essential for the healthy operation of a turbine. However, other parameters controlling the leakage fraction can be varied. For instance, increasing the number of seals reduces the pressure difference over each seal and hence the leakage flow rate. Xiao et al. [24] showed with the help of a two dimensional simulation of a shroud leakage channel that the leakage flow rate varied as the number of seals to the power of -0.45. An implementation of shroud swirl [25] in their simulation reduced the leakage flow rate by only 2 percent. It was also observed that the leakage flow increased as the square root of the overall pressure difference. Since they had a radially staggered arrangement of the seals, the leakage flow rate was not seen to be influenced much by the distance between the seals. However, in a 'see-through' seal configuration, placing the seals too close together would result in a kinetic energy carry-over of the leakage jets under the seals. This would increase the leakage flow rate.

2.4.2 Shroud/Casing Geometry

The mixing inside cavities and the leakage fraction can both be reduced by making appropriate changes to the shroud and casing geometry. This was shown by Rosic et al. [8] who numerically modified a three-stage low speed turbine and made the following conclusions for their particular shroud configuration:

- The exit cavity length should be small because it reduces the in-cavity mixing and the leakage fraction.
- A shroud overhang in the exit cavity is beneficial only when it is very big so that the reduction in the bulk flow ingress starts to dominate the increase in strength of the leakage jet and the increase in the windage loss.
- The inlet cavity length should be small because it reduces the in-cavity mixing, the leakage fraction, and the cavity influence on the bulk flow. For the same reasons, the shroud overhang in the inlet cavity should be as big as possible.
- The shroud thickness should be small because it lowers the leakage fraction due to the increased difficulty of the leakage flow in passing through the first seal fin and a higher dissipation of the leakage jet inside the larger cavities.
- The shroud cavity depth should be small. It is because although the reduced cavity depth increases the kinetic energy carry-over of the leakage jets, this effect is outweighed by the reduction in the in-cavity mixing. However, the exit cavity depth should be chosen carefully. A small depth reduces the in-cavity mixing but causes the leakage jet to directly propagate towards the downstream row, thus increasing its secondary flows. This phenomenon was also observed by Schlienger et al. [26] in their tests on a two-stage low speed turbine.

In order to reduce the impact of the re-entering leakage flow on the downstream row, non – axisymmetric end wall profiling, as proposed by Pfau et al. [27], can be used at the following locations:

- The shroud leading edge, so as to reduce the bulk flow ingress to the inlet cavity near the blade pressure side and increase it near the suction side.

- The shroud under the last seal tooth, which would direct the leakage jet preferentially on the blade wake and thus increase the flow uniformity over the downstream row.
- The casing behind the exit cavity, to direct the leakage flow onto the downstream blade suction surface, which would reduce secondary flow formation.

Since the leakage flow is driven by the pressure difference across the blade row, some authors suggest that introducing loss in the inlet cavity may help to reduce the leakage flow rate whereas the exit cavity should be designed to maximize the exit cavity static pressure ([22], [28]).

2.4.3 Exit Cavity Shaping

A few researchers in the past have considered shaping the exit cavity to improve the leakage flow re-entry into the bulk flow. Rosic et al. [28] made various modifications to the exit cavity geometry of a three-stage low speed turbine. The various changes and their impact on the predicted and measured turbine efficiency are summarized in Table 1. Using the results from this table and the study on the shroud and casing geometry described earlier [8], an optimized leakage channel geometry was also designed by [28]. It consisted of a combination of a reduced shroud thickness, a reduced inlet cavity depth, a shroud overhang in inlet cavity, a radial deflector and a chamfered cavity. When it was tested numerically, a total-to-total efficiency improvement of 0.75 percent was realized. However, no experimental study was performed on the optimized geometry as it required a significant modification to the existing turbine test rig of the Whittle Laboratory.

A new flow feature referred to as the "leakage vortex" was identified by Adami et al. [14] through unsteady CFD of a typical high pressure 1.5 stage turbine. This vortex was formed as a result of the shear between the re-entering leakage flow ((**C**) in Figure 2) and the bulk flow. In the case of the sharp cavity edge, there was a flow separation at the edge. As a result, there was a recirculation in this region, and a significant difference existed in the axial velocities of the recirculating fluid and the bulk flow. So, the shear in this case was due to the differences in the axial velocity as

well as the tangential velocity. Chamfering the exit cavity removed the separation seen in the case of the sharp cavity edge, which made the shear primarily a result of the tangential velocity difference. Hence, the shear was reduced and the leakage vortex was weakened in the chamfered exit cavity case.

Modification	Δη (%)	Reason
Chamfered cavity: 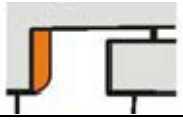	EXP: -0.08 CFD: +0.03	• Reduced radial velocity component of re-entry leakage jet.
Contoured cavity: 	EXP: +0.19 CFD: +0.16	• Reduced radial velocity component of re-entry leakage jet. • Lower main flow ingress. • Reduced swirl of leakage jet due to its increased mixing with main flow.
Straight axial deflector: 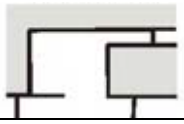	EXP: +0.11 CFD: +0.27	• Smaller mainstream fluid ingress.
Inclined axial deflector: 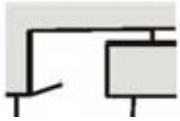	EXP: +0.36 CFD: +0.43	• Minimized mainstream fluid ingress. • Smaller separation region downstream of exit cavity. • Reduced swirl of leakage jet due to its increased mixing with main flow.
Circular axial deflector: 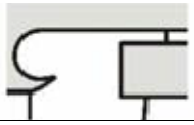	EXP: Not implemented CFD: +0.25	Same as for the inclined axial deflector.
Radial deflector A: 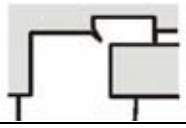	EXP: Not implemented CFD: +0.35	• Leakage jet redirected towards exit cavity centre. • Minimized flow separation downstream of exit cavity.
Radial deflector B: 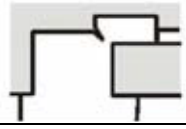	EXP: Not implemented CFD: +0.29	• Smaller leakage fraction due to additional seal fin.
Radial deflector C: 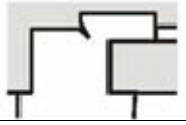	EXP: Not implemented CFD: +0.24	• Leakage jet redirected towards exit cavity interior.

Table 1, Exit Cavity Modifications by Rosic et al. [28]

2.4.4 Turning Device

Some authors have tried to turn the leakage flow in the direction of the bulk flow in an attempt to reduce the re-entry mixing loss and the downstream impact. For example, Wallis et al. [22] placed bladelets on the rotor shroud of a four-stage low aspect ratio turbine. However the efficiency was seen to drop by 3.5 percent. The reason was that, as the thick bladelets were placed on the shroud, they were creating a blockage for the leakage flow. This was enhancing the periodic ingress and egress of the flow at the inlet and exit cavities due to the underlying rotor blade potential field. It was also preventing the formation of a strong leakage jet at the exit cavity which would act as an "air curtain" and prevent main flow ingress here.

So, rather than having bladelets on the shroud, Rosic et al. [29] placed turning vanes near the downstream edge of the exit cavity. These vanes were shaped to collect the leakage flow from the last seal fin and direct it towards the bulk flow before mixing with it. A significant improvement was observed in the yaw angle and the mixing loss at the rotor exit. As a result, an improvement in the turbine brake efficiency of 0.4% was noted for the design condition. However, the turning vanes were seen to hinder the rotor axial movement.

A comparison between turning vanes and exit cavity chamfering was performed by Gao et al. [30] in their simulations of a 1.5-stage high aspect ratio turbine. They compared the mixing losses at the rotor exit and showed that exit cavity chamfering led to a better performance. It remained to be seen however if an increase in the number of turning vanes could produce a further reduction in losses. No study was performed on a case that combined turning vanes with a chamfered cavity.

2.4.5 Fluidic Jet Barriers

Although the concept of fluidic jet barriers to control turbine tip leakage is over six decades old, it has received a renewed attention by researchers only in recent years. This interest is the result of an increased awareness of the limitations of conventional labyrinth seals, such as their mechanical integrity issues. However, few researchers

have focused on fluidic jets and so there are only a handful of publications on this concept.

Curtis et al. [2] implemented such a jet in their experiments on a single-stage low speed air turbine. They found that increasing the jet flow decreased the leakage flow by a similar amount. As the jet pressure was raised, initially there was a 0.6 percent improvement in the turbine efficiency. But once the jet mass flow had crossed 1.2 percent of the bulk flow, the efficiency started decreasing exponentially. The reason was that initially the increase in the turbine work had a bigger influence on the efficiency, but later the increase in turbine work was outweighed by the energy supplied to the jet.

Hogg et al. [3] explored fluidic jets by way of two-dimensional CFD. First, a simple case of a jet injected into a channel was investigated, but only a slight reduction in the channel outlet mass flow rate was observed. Then a second case was tested where the fluidic jet was implemented on a conventional labyrinth seal with minimal modifications to its design. This time a reduction of approximately 25 percent in the outflow was recorded. Messenger [31] also reported a similar flow reduction in his CFD analysis of an annular fluidic seal test rig.

Auld et al. [4] extended the work of Hogg et al. [3] by performing two-dimensional simulations of a turbine shroud leakage channel with a fluidic jet. Several computations were conducted to determine the optimum location, width and angle of the jet. After taking into account the leakage mass flow reduction and the shroud shear force, the optimum jet predicted a net power increase of up to 3.5 percent.

So the domain of fluidic jet barriers is still relatively unexplored and it is the aim of this thesis to carry the study forward in this area.

3 Leakage Loss Reduction

This chapter makes a case for investigating fluidic jets by describing the various ways in which they can help to reduce leakage loss in shrouded turbines.

3.1 Denton's Entropy Model

The mixing between the re-entering leakage flow and the bulk flow is a significant contributor to the shroud leakage loss. Gier et al. [12] numerically simulated the flow in a three-stage aero engine low pressure turbine with hub and shroud cavities and showed that almost 50 percent of the leakage loss was generated by the mixing at re-entry. Therefore it makes sense to focus on this particular loss component when thinking of leakage loss reduction techniques.

Shapiro [32] presented a theory for the entropy rise of a mainstream flow when a small quantity of fluid is injected into it:

$$\Delta s = \left(c_P \frac{\dot{m}_f}{\dot{m}_m}\right)\left[\left(1 + \frac{\gamma - 1}{2} M_m^2\right)\frac{T_{0f} - T_{0m}}{T_{0m}} + (\gamma - 1)M_m^2\left(1 - \frac{V_f \cos\alpha}{V_m}\right)\right] \qquad (1)$$

where $\dot{m}_f$ is the injection mass flow rate, V_f is the injection velocity, α is the injection angle, T_{0f} is the injection total temperature, $\dot{m}_m$ is the mainstream mass flow rate, M_m is the mainstream Mach number, T_{0m} is the mainstream total temperature, γ is the ratio of specific heats and c_P is the specific heat of air.

Denton [1] used the above theory to formulate an analytical model to estimate the rise in the entropy of the bulk flow when the turbine shroud leakage flow re-enters the bulk flow. By assuming the same stagnation temperatures for the leakage flow and the bulk flow, and applying the theory independently in the axial and the tangential directions, he showed that:

$$T\Delta s = \left(\frac{\dot{m}_L}{\dot{m}_m}\right)\left[V_{y2}^2\left(1 - \frac{V_{yL}}{V_{y2}}\right) + V_{x2}^2\left(1 - \frac{V_{xL}}{V_{x2}}\right)\right] \qquad (2)$$

where $\dot{m}_L$ is the leakage mass flow rate, $\dot{m}_m$ is the bulk mass flow rate, V_{yL} is the tangential velocity of leakage flow, V_{y2} is the tangential velocity of bulk flow, V_{xL} is the axial velocity of leakage Flow and V_{x2} is the axial velocity of bulk flow.

From equation (2), it can be deduced that, in order to lower the re-entry mixing loss, the following quantities should be minimized:

- The leakage mass flow re-entering the bulk flow
- The difference between the tangential velocities of the leakage flow and the bulk flow
- The difference between the axial velocities of the leakage flow and the bulk flow

As shown below, fluidic jets have the potential to fulfill all of these conditions.

3.2 Fluidic Jet Potential

3.2.1 Leakage Flow Rate Reduction

Figure 5 shows a simple schematic where a fluidic jet is implemented on a shrouded rotor configuration. As shown in Figure 5, when the jet is injected at an angle (θ) against the leakage flow, it is turned towards the direction of leakage (**A**) which requires a force. Thus there has to be a pressure drop across the jet such that the pressure upstream of the jet is raised (**B**) whereas the downstream pressure is lowered (**C**). Since the driving force of the leakage flow is the pressure difference across the blade passage, it now sees a smaller pressure difference and so the mass flow entering the leakage channel ($\dot{m}_i$) is reduced. In this way, more fluid passes through the blade passage and there is an increase in the blade work.

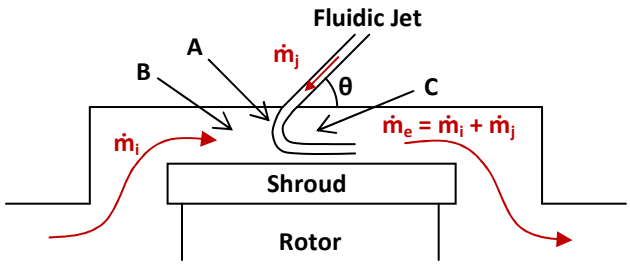

Figure 5, Fluidic Jet Principle

3.2.2 Mixing Loss Improvement

In order to be able to reduce the mixing loss at re-entry, the fluidic jet needs to meet the requirements of Denton's equation.

Continuity dictates that the total mass flow rate re-entering the bulk flow is the sum of the leakage and the jet mass flow rates, i.e., $\dot{m}_e = \dot{m}_i + \dot{m}_j$. As stated previously, the studies by Hogg et al. [3], Messenger [31] and Auld et al. [4] have already demonstrated the ability of fluidic jets to reduce this re-entering mass flow rate ($\dot{m}_e$). So this satisfies the first requirement of Denton's equation.

In the few published works on fluidic jet barriers, the main focus has been to block the leakage flow and increase the turbine work. They are not concerned with the re-entry mixing loss. However, in the present study, the jet is injected with an additional tangential component in the direction of the blade exit bulk flow, so that it can turn the re-entering flow in that direction. This is intended to reduce the difference in the tangential velocities of the two mixing fluids. In turbine shroud leakage cases, the tangential velocity difference is much bigger than its axial counterpart, and so has a much higher contribution to the mixing loss. So this jet manipulation would result in a net reduction in the re-entry mixing loss. The axial component of the jet would still act to reduce the re-entering flow rate. In this way, all the conditions of Denton's equation are fulfilled.

A two-fold benefit of leakage reduction and mixing loss improvement is, therefore, theoretically possible from the employment of fluidic jet barriers. The present thesis seeks to explore these ideas.

4 CFD Validation

Computational Fluid Dynamics (CFD) was the main technique applied in the present study. Although CFD tools have made significant advances over the last decade, there are still some limitations of modern CFD when applied to turbomachinery. Denton, in his 2010 publication [33], after taking into account the various sources of error, concluded that it should primarily be used for understanding the flow physics rather than looking for the absolute performance numbers. He also mentioned that it is possible to look at the numbers but only when used on a comparative basis. Since the present study mainly involved flow physics comprehension and performance comparison, CFD was considered an appropriate technique.

4.1 Leakage Flow Analysis Cascade

The CFD methodology that was employed in this study was first validated against experimental data. Earlier, as part of a commercial testing project, measurements had been conducted by the author on a leakage flow analysis cascade at Durham. It is a linear (as opposed to an annular) cascade to study the interaction of the shroud leakage flow with the bulk flow in a turbine rotor. Figure 6 shows a meridional view of the cascade.

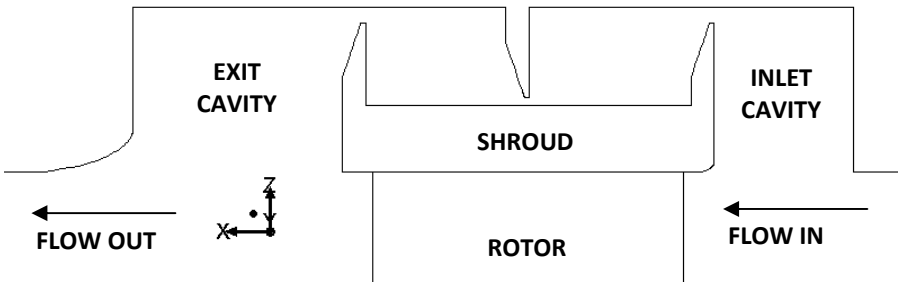

Figure 6, Leakage Flow Analysis Cascade Meridional View

The cascade has six blades which are numbered from top to bottom as '-3', '-2', '-1', '+1', '+2' and '+3'. Tailboards were used on either side of the cascade exit flow, and their angle was set to give the best pitchwise periodicity of the flow. The cascade blade profile was taken from a typical short height turbine stage. Elliptical fillets were applied on the shroud leading edge and the exit cavity rear edge to prevent

flow separation in these regions as in common industrial practice. The main geometrical parameters of this cascade are given in Table 2.

Inlet Flow Angle (β_1)	2.3°
Turbulence Intensity	4%
Exit Flow Angle (β_2)	-76.1°
Blade Axial Chord (C_x)	88 mm
Blade Pitch	135.56 mm
Blade Span	375 mm
Inlet Velocity	12 m/s
Re	2.78×10^5

Table 2, Leakage Flow Analysis Cascade Parameters

The experimental campaign involved pneumatic measurements using 5 hole and 3 hole pressure probes. The 5 hole probe head diameter was 3 mm, and it was used to take data up to 10 mm from the end wall. The 3 hole probe head was less than 3 mm across the holes and 0.8 mm wide, and it captured data from 10 mm to 1mm from the end wall. The probes were first calibrated using an in-house calibration facility at Durham. Then the measurements were taken at several locations at the cascade exit using a three-axis automated probe traverse system. In this way, a detailed map of the cascade exit flow was obtained

4.2 Computational Technique

4.2.1 Meshing Strategy

The computational mesh used for the CFD modeling of the leakage flow analysis cascade is illustrated in Figure 7. One blade passage was modeled and a fully structured mesh was generated using the commercial software Pointwise. The flexibility of this meshing tool allowed for structured grids for both the shroud leakage channel as well as for the blade-to-blade passage.

An O-grid topology was used around the blade whereas the blade-to-blade passage was meshed using an H-grid. For a grid cell, equiangle skewness is a measure of how

far it is from the ideal (equiangular) cell. Its value ranges from 0 for the ideal cell to 1 for the worst cell. Mesh quality was maintained by keeping the maximum equiangle skewness of the cells to 0.6 and the cell growth ratio below 1.3.

In CFD, only a properly resolved near-wall region can produce realistic features such as separation and the three-dimensionality of the boundary layer. So the wall y^+ value was below 1 for all walls. This ensured that the near-wall flow was well resolved in space. The total grid size was approximately 3.6 million cells. Time constraints did not permit a formal grid independence check in the present study, so the results could be grid dependent. However, the fact that the mesh was based on best practice criteria, and that the grid size for the present single rotor was either comparable to or larger than the multi-stage shrouded turbine meshes used in the past studies ([12], [17], [21]), gave confidence that the mesh was sufficiently resolved.

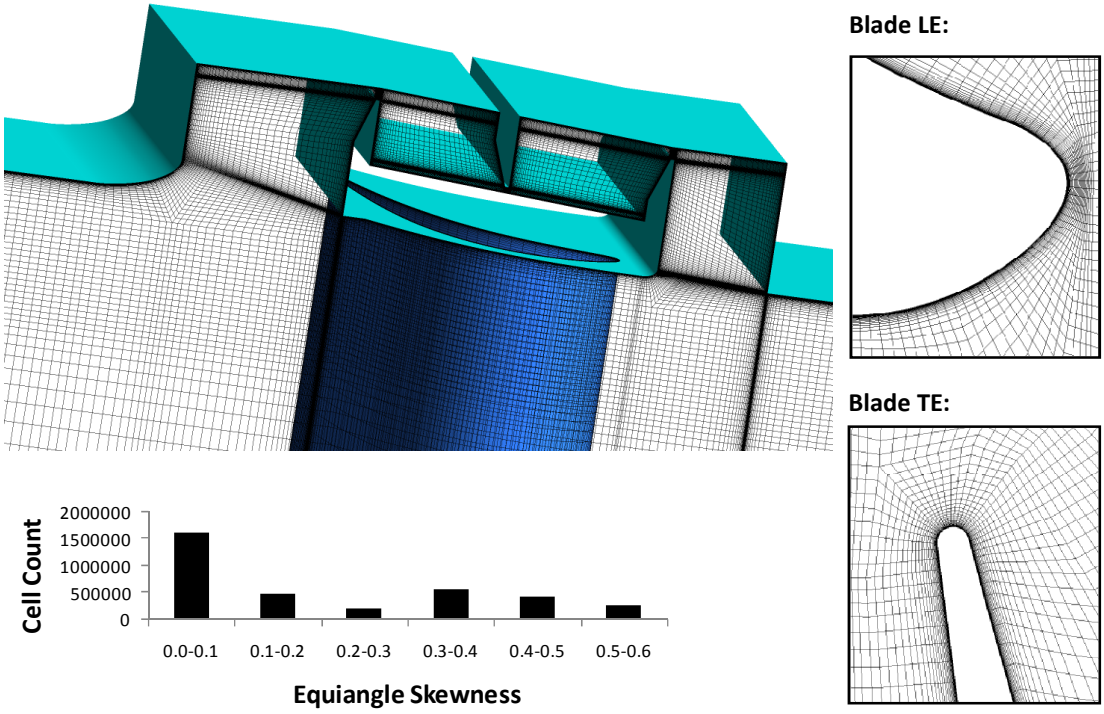

Figure 7, Leakage Flow Analysis Cascade Mesh

4.2.2 Boundary Conditions

The total pressure and the inflow angle were imposed at the inlet boundary to give the same inlet flow velocity and direction as in the experiment. The atmospheric

pressure condition was applied at the outlet. The working fluid for this low speed incompressible case was air at a constant density. Turbulence intensity and length scale were specified from hotwire measurements during the previous cascade tests. Since the purpose was to simulate a linear cascade, translational periodicity was applied across the domain. The solution was initialized by imposing a uniform axial velocity throughout the computational domain.

4.2.3 Solution Methods

Fully three-dimensional simulations were conducted using the commercially available solver Ansys Fluent 14.0. It is a widely used product which solves the Reynolds Averaged Navier Stokes (RANS) equations using the finite volume approach. The continuity and momentum equations were solved using the SIMPLE pressure-based method to produce a converged steady flow solution. The solver was run in parallel mode on four cores and a convergence was achieved within 24 hours. Five different turbulence models were tried: Standard k-ε, Realizable k-ε, RNG k-ε, k-ω SST and Transition SST.

It may be noted that the near-wall mesh refinement results in some cells being placed inside the viscous-sub-layer of the boundary layer. But the ε equation cannot be integrated directly through the viscous sub-layer. For this reason, the Enhanced Wall Treatment (EWT) feature was activated for all the k-ε based models, which smoothly blends the viscous sub-layer formulation with the logarithmic layer formulation.

The parameters observed to judge convergence were:

- The scaled residuals of continuity, momentum and energy were at least 10^{-5}.
- The standard deviation of a quantity is a measure of its variation about the mean value. When it is expressed as a percentage of the mean value it is known as the relative standard deviation. Over the last 1000 iterations, the mass-averaged total pressure and the mass flow rate at the outlet showed relative standard deviations of 0.000007% and 0.000004% respectively. This indicated that the above quantities had almost become constant and provided further confirmation of convergence.

4.3 Validation

4.3.1 Pitch Mass-averaged Results

Pitch mass-averaged results from the CFD were compared with the experiment along the radial direction. The comparison was made at two axial locations downstream of the cascade trailing edge. Taking the blade leading edge as the origin, these locations were referred to as:

- **1.1C_x** or 0.1 axial chord behind the blade trailing edge.
- **2.5C_x** or 1.5 axial chords behind the blade trailing edge.

The 2.5C_x location was at a significant distance along the flow from the trailing edge. This meant that any deviation from pitchwise periodicity was amplified here. So, test data for both the central wakes '-1' and '+1' was included in this comparison. Figure 8 and Figure 9 show these results for locations 1.1C_x and 2.5C_x respectively. The variables involved in the comparison were the total pressure loss coefficient and the non-dimensional components of the velocity.

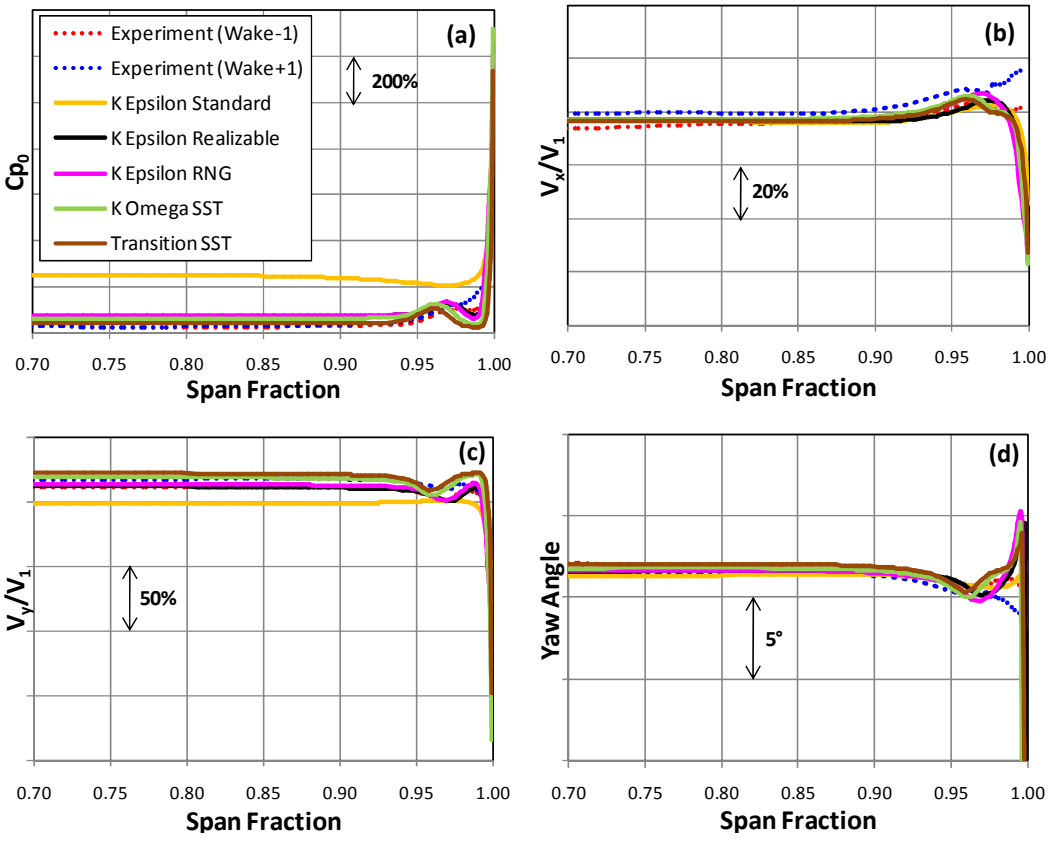

Figure 8, CFD vs. Experiment: Pitch Mass-averaged Results at 1.1C_x

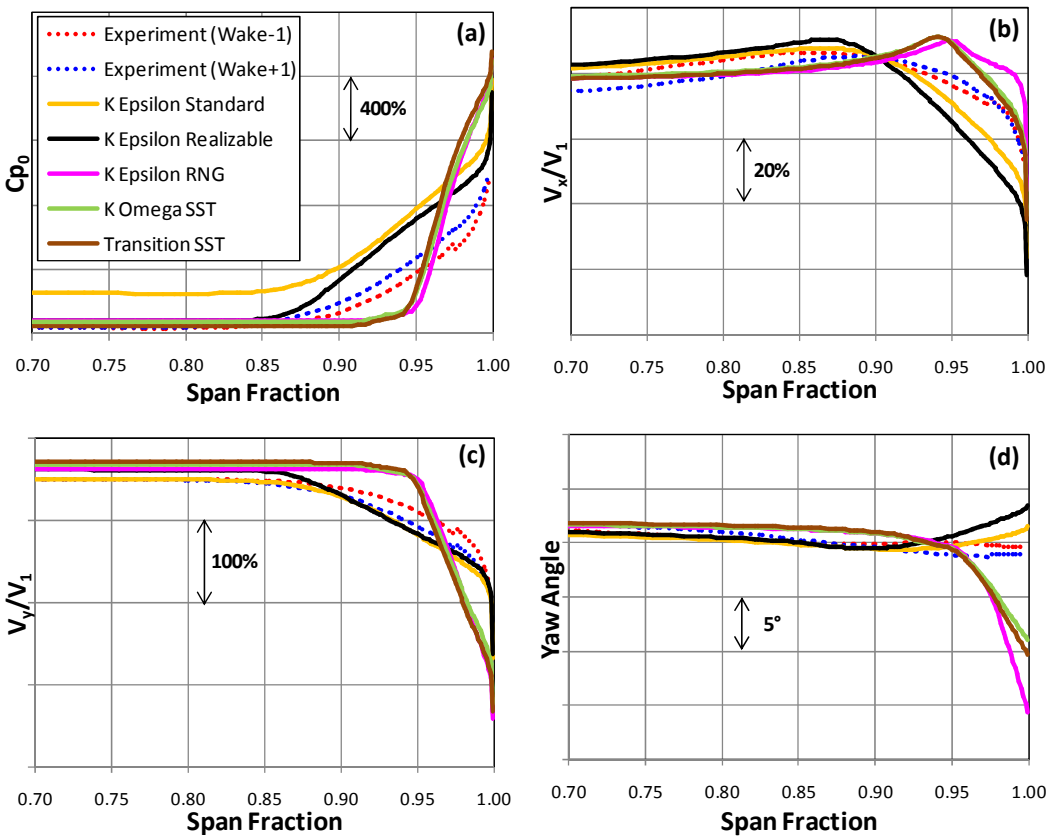

Figure 9, CFD vs. Experiment: Pitch Mass-averaged Results at 2.5C_x

The total pressure loss coefficient was defined as follows:

$$Cp_0 = \frac{P_{01} - P_0}{P_{01} - P_{s1}} \tag{3}$$

where P_{01} is the inlet total pressure, P_0 is the local total pressure and P_{s1} is the inlet static pressure. The following observations were made at 1.1C_x:

- The Standard k-ε model produced a higher loss (Cp_0) and a lower turning (V_y/V_1) compared to the other models, as shown in Figure 8(a) and Figure 8(c) respectively. It was because the turbulence production term in this model is insensitive to streamline curvature by default and so a curvature correction coefficient needs to be specified. As an indication of this, a high loss was seen to develop on the highly curved blade suction surface. Increasing the curvature correction coefficient reduced this loss, but it was difficult to determine its most appropriate value. The losses and turnings predicted by all the other models were closer to the experimental values.

- Because this location was upstream of the exit cavity, there was no leakage loss here. So the only losses seen here were the secondary flow and the wake losses. The secondary loss from the Transition SST model showed the best agreement with the experiment, as indicated in Figure 8(a). All the other models showed a slightly higher value. This could be because the other models assumed a fully turbulent boundary layer everywhere. Since this was a low Reynolds number case, the boundary layer in the experiment was most probably transitional and this feature is only accounted for in the Transition SST model. The transitional state of the boundary layer for the Transition SST model could also explain its closest agreement with the experiment in Figure 8(a) in terms of a more accurate prediction of the wake loss.
- Secondary flows produce deficits in the axial velocity and the tangential velocity close to the blade tip, at span fraction = 1. The extent of these reduced axial velocity and tangential velocity zones was captured more correctly by the SST models, as shown in Figure 8(b) and Figure 8(c) respectively. As a consequence, they showed a closer match with the experiment in terms of the yaw angle distribution in the secondary flow region (Figure 8(d)).
- The axial velocity (V_x/V_1) in Figure 8(b) shows differences between the CFD and the experiment near the end wall. The reason for this could partly be experimental error due to a slightly different yaw alignment of the 3 hole probe in the experiment which returned a higher axial velocity in the near wall region. This resulted in a slightly different yaw angle distribution for the experiment compared to the CFD near the casing, as shown in Figure 8(d).

At $2.5C_x$, these observations were made:

- This location was well behind the exit cavity and downstream of the start of the interaction between the re-entering leakage flow and the bulk flow. This is the reason for the higher loss seen near the end wall in Figure 9(a). The secondary flow loss cannot be separated from the leakage loss in this region. Again the Standard k-ε model shows a higher loss and a lower turning for the reason stated earlier.

- Figure 9(a) shows that the RNG k-ε and the SST models predicted a region of high loss close to the blade tip that has a lower radial spread than in experiment. This could be because, in rapidly strained flows, such as the case of leakage flow interaction with the bulk flow, all these models yield a lower turbulent viscosity. This leads to the confinement of the leakage flow interaction close to the casing, due to the reduced eddy diffusivity. The reduction in mixing by the lower eddy viscosity is such that, at the end wall, the loss and the underturning predicted by these models were much higher than that of the experiment.
- The Realizable k-ε model imposes certain mathematical constraints on the Reynolds stresses to maintain the turbulent viscosity within realistic levels in rapidly strained flows. This resulted in a lower increase in loss approaching the casing wall that was a closer match to the experimental trend. The loss distribution predicted by this model matched most closely with the experiment among the closure models tested.
- The Standard k-ε model does not modify the turbulent viscosity for rapidly strained flows. It was interesting to note that, notwithstanding the high level of loss, the trend observed in experiment of a monotonic loss increment approaching the casing wall was most closely captured by this model. This was also the case for the comparison between the measured and predicted radial velocity distribution shown in Figure 9(b-d). However, the difference between the profile loss predicted and measured towards the blade mid-span prevented its selection as the most suitable model.
- In the region of leakage interaction, the experiment showed a lower loss and a higher axial velocity than the Realizable k-ε model. This was most likely to be a CFD prediction error. Alternatively, it could be because clearance measurements during the experiment had revealed that they were slightly higher compared to the original design. This would mean an increased leakage flow rate and so, more energized flow near the end wall for the experiment.

Since the present study was on leakage interaction, the results at $2.5C_x$ were given more importance than those at $1.1C_x$. So from the above observations, the Realizable k-ε model was seen to best represent this interaction. Next it was intended to have an idea of the Realizable k-ε model's accuracy. For this, the pitch mass-averaged values were used to calculate the errors for the different variables at $2.5C_x$. Errors were estimated from $\varepsilon = (\varphi_{CFD} - \varphi_{exp})$, where φ is the scalar variable being compared. Errors are calculated from both the central wakes separately and are plotted in Figure 10. Here it should be kept in mind that the errors might be exaggerated because of the higher clearances in the experiment.

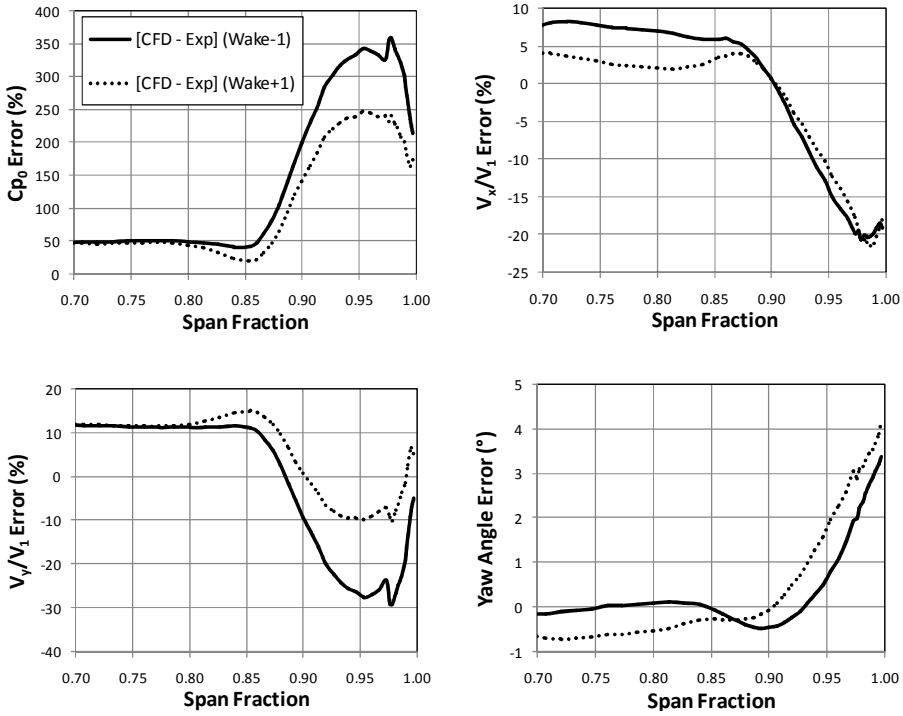

Figure 10, CFD Prediction Errors at $2.5C_x$

These CFD errors can have the following implications on the results presented in this thesis: Within the mid-span region, the CFD can be expected to slightly over-predict the loss and the axial and tangential velocities. The yaw angle error should be within ±1°. In the leakage interaction region, the errors are likely to be higher. Here, one can expect the loss to be over-predicted whereas the axial and tangential velocities to be under-predicted. The yaw angle prediction can be higher than the actual value by up to 5°.

4.3.2 Leakage Fraction

For a simulation on leakage interaction, it is also important to predict the leakage fraction correctly. The leakage fraction is the leakage mass flow as a percentage of the blade bulk flow. Such a comparison is shown in Table 3. It may be noted that, before the start of the test campaign, the cascade was disassembled in order to incorporate some modifications, after which the aforementioned increase in clearances was observed. However, the experimental leakage fraction was measured during a previous test campaign and so the clearances at that time were the same as the design value. Again, Realizable k-ε showed one of the closest agreements with the experiment with a slight under-prediction of 0.03% in leakage fraction. This corresponds to a discrepancy of 0.03/1.32 ≈ 3% in leakage fraction between the results from the Realizable k-ε model and the experiment.

Experiment	1.32
Standard k-ε	1.38
Realizable k-ε	1.29
RNG k-ε	1.30
k-ω SST	1.23
Transition SST	1.25

Table 3, CFD vs. Experiment: Leakage Fractions (%)

Thus it was deduced that Realizable k-ε was the most suitable turbulence model for the present study. The agreement observed in these validation tests gave confidence in the CFD methodology. Hence, the same mesh settings were used for the fluidic jet study. The mesh quality and cell count were also kept similar to the validated case. With the computational technique established, it was possible to proceed to the main body of the present work.

5 The Baseline Case

To assess the fluidic jet impact, first a baseline case was designed as a reference case. It did not include a fluidic jet and consisted only of a shrouded rotor blade with a leakage channel passing over it. The purpose of the baseline case was to represent a typical industrial shrouded rotor configuration. There were two reasons for this design philosophy:

- To assess the feasibility of fluidic jet inclusion within the geometric constraints of a modern turbine.
- To have a direct indication of the impact that the fluidic jet would have on a representative turbine design.

5.1 Geometry

The existing so-called Durham Cascade [34] has prismatic blades with a blade profile taken from a high pressure turbine rotor design, so this blade profile was considered appropriate for the present study. Table 4 contains details of the Durham Cascade. The rotor shroud and the leakage channel were based on a best practice design of shrouded turbines currently used in the power generation industry. The dimensions were kept in some proportion to the blade axial chord (C_x). Figure 11 shows a meridional view of the baseline case with the associated dimensions.

Inlet Flow Angle (β_1)	42.75°
Turbulence Intensity	5%
Exit Flow Angle (β_2)	-68.7°
Blade Axial Chord (C_x)	181 mm
Blade Pitch	191 mm
Inlet Velocity	19.1 m/s
Re	4.0×10^5

Table 4, Durham Cascade Parameters

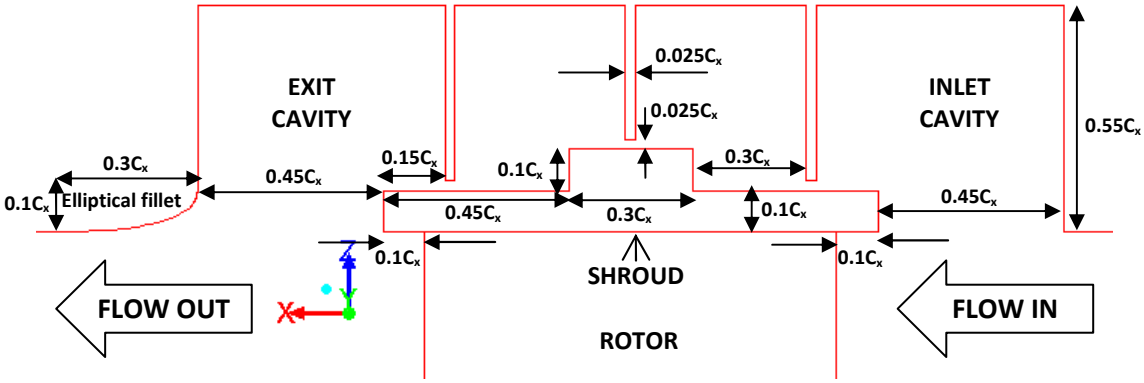

Figure 11, Baseline Case Geometry with Dimensions Relative to the Axial Chord C_x

5.2 Meshing

The baseline case was meshed using the same guidelines as described in the 'CFD Validation' chapter. Both the leakage channel and the blade passage had a fully structured grid with the cell growth ratio below 1.3 and the wall y^+ value below 1 for all walls. The maximum equiangle skewness was just over 0.6 and the total grid size was approximately 4.9 million cells. The higher cell count compared to the validation case was because of the different seal design which involved more cells within the leakage channel. This increased the time required for convergence to about 48 hours. The mesh for the baseline case is illustrated in Figure 12.

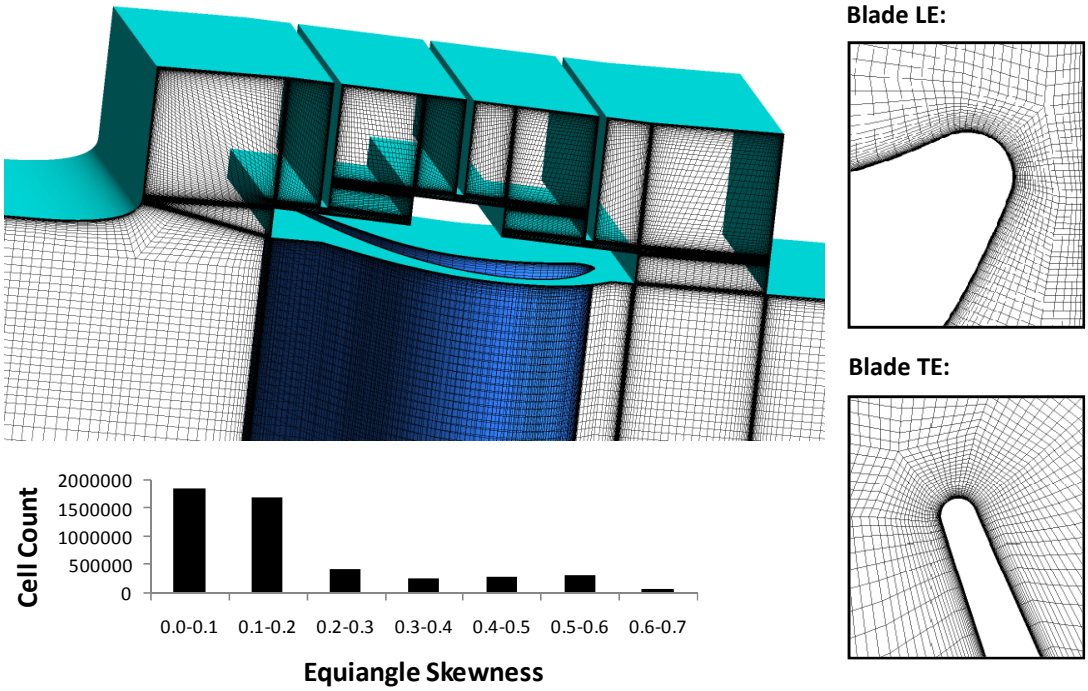

Figure 12, Baseline Case Mesh

5.3 Blade Velocity

In order to represent the rotor tip flow through a real turbine, a velocity was imparted to the blade and the shroud, while the casing was kept stationary. As the blade profile was taken from a linear cascade, a translational velocity was applied. In order to calculate the blade velocity, the velocity triangle at the rotor inlet was drawn as shown in Figure 13.

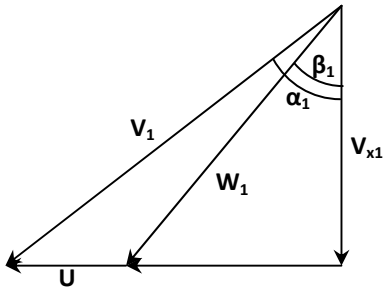

Figure 13, Rotor Inlet Velocity Triangle

From the triangle,

$$V_1 \cos \alpha_1 = W_1 \cos \beta_1 = V_{x1}$$

So, $$V_1 = W_1 (\cos \beta_1 / \cos \alpha_1) \quad (4)$$

Also, $$V_1 \sin \alpha_1 = U + W_1 \sin \beta_1 \quad (5)$$

Substituting (4) into (5),

$$W_1 \cos \beta_1 \tan \alpha_1 = U + W_1 \sin \beta_1$$

So, $$U = W_1 (\cos \beta_1 \tan \alpha_1 - \sin \beta_1)$$

$$= 19.1 (\cos 42.75° \tan 70° - \sin 42.75°)$$

$$= 19.1 (1.339) = 25.5749 \text{ m/s}$$

The above flow velocities and angles were taken from the Durham Cascade parameters shown in Table 4. The rotor absolute inlet angle of 70° was an assumption based on general industrial turbine practice.

5.4 Boundary Conditions

The inlet boundary condition was not straightforward. Initially, an absolute total pressure of 103118 Pa at an absolute angle of 70° was imposed at the inlet. This gave a relative inlet velocity of 19.1 m/s, the same as the Durham Cascade. However, when the same total pressure was applied to the fluidic jet cases, there was a drop in the inlet mass flow rate. The reason for this was the blockage effect created by the fluidic jet. So instead of a total pressure, a mass flow rate was specified at the inlet for all cases. A summary of the approximate number of test runs performed before arriving at the final set of boundary conditions is presented in Table 5.

Case	No. of Runs	Reason
Baseline Case	10	To arrive at the inlet total pressure corresponding to the correct relative inlet velocity.
Baseline Case	1	To change inlet boundary condition to mass flow inlet.
Fluidic Jet Cases	5	To arrive at the minimum jet pressure required to overcome the reversed flow at jet inlet.
Fluidic Jet Cases	5	To determine the minimum jet pressure required for the overblown condition.
Fluidic Jet Cases	1 to 2	The intermediate pressure case.

Table 5, Summary of Test Runs

Atmospheric pressure was applied at the outlet. The simulations were treated as incompressible because, even for the fluidic jet cases, the highest jet velocities reached were of the order of Mach 0.2. So, air at a constant density of 1.225 kg/m^3 was used as the working fluid. Previous hotwire measurements in the cascade provided the turbulence intensity and length scale which were 5% and 0.936mm respectively [35]. These values were set at the inlet and the outlet boundaries. Translational periodicity was specified across the domain, as required by the present linear cascade.

5.5 Flow Features

Figure 14 shows contours of the relative total pressure loss coefficient on a meridional plane for the baseline case. Streamlines are also shown to illustrate the flow inside the cavities. The relative total pressure loss coefficient was defined using the relative values of velocity, i.e., in the frame of reference of the moving blade, as:

$$Cp_{0,rel} = \frac{P_{01,rel} - P_{0,rel}}{P_{01,rel} - P_{s1}} \tag{6}$$

where $P_{01,rel}$ is the inlet relative total pressure, $P_{0,rel}$ is the local relative total pressure and P_{s1} is the inlet static pressure. The relative quantity was considered appropriate to illustrate the flow features because, in the absolute reference frame, there was a drop in the total pressure across the rotor due to work extraction by the rotor. However, this was an inviscid mechanism whereas the present intention was to look only at the viscous effects. The main features of the baseline case were:

- A portion of the incoming flow was sucked into the inlet cavity. Some of this ingested fluid passed under the seal tooth (**A**) and the remaining fluid re-entered the main passage after forming a big vortex inside the inlet cavity (**B**).
- The leakage flow formed several vortical structures as it passed under the successive teeth (**C**). There was a sharp rise in the loss coefficient after each tooth (**D**) and this was normal because the purpose of the seal was to induce losses and hence reduce the leakage mass flow. The leakage fraction was a little over 1 percent. This was within the range of 1 – 4 percent which is generally found in industrial HP steam turbines [8].
- A high loss region was seen where the leakage jet came out of the last tooth and re-entered the bulk flow (**E**). This was due to the mixing between the two flows and a thick layer of low energy fluid was formed downstream of the mixing region (**F**). Some of the leakage flow also formed a large vortex inside the exit cavity (**G**). A small portion of the bulk flow entered the space under the leakage jet just behind the shroud trailing edge and formed two small vortices, one on top of the other, sticking to the shroud trailing edge (**H**).

- Within the bulk flow, other flow features associated with turbines such as the blade wakes (**I**) and the secondary flows (**J**) were visible. Due to the lower pressure on the wake suction side, the leakage flow was able to penetrate more in this region and was seen like a bump on the low energy layer boundary (**K**). This was the reason for the low energy fluid layer showing a wavy boundary structure.

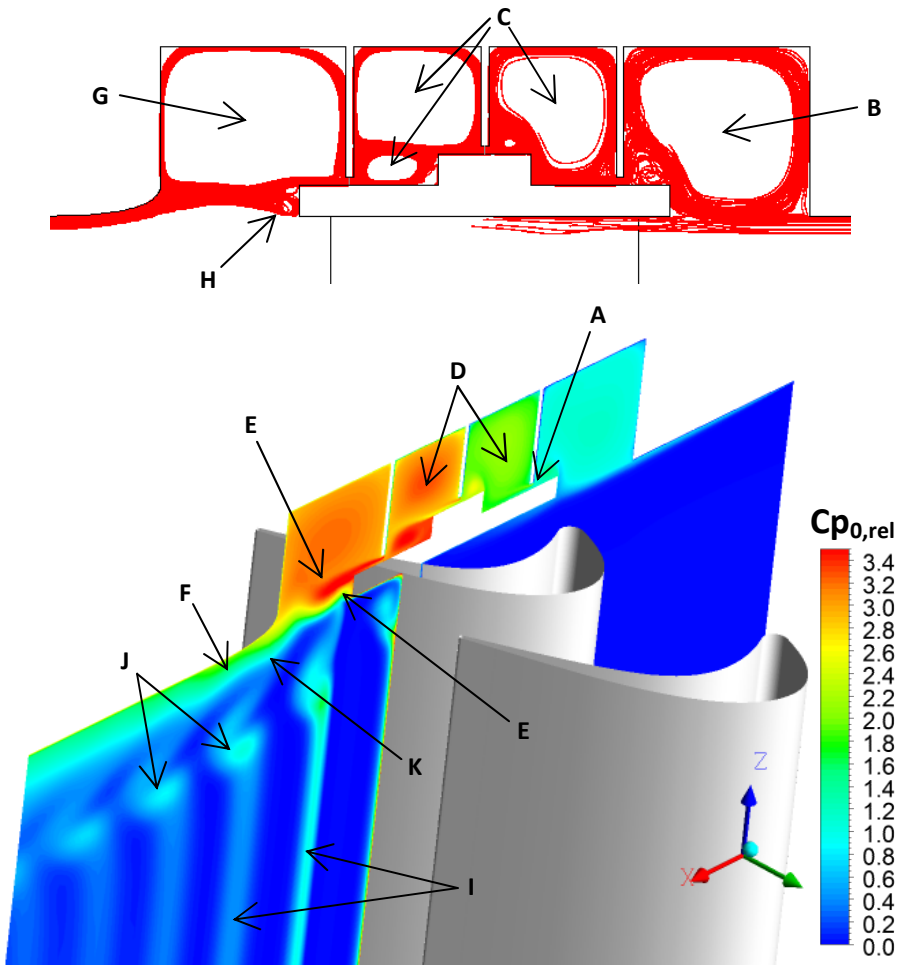

Figure 14, Baseline Case: Loss on the Meridional Plane

The entropy generation rate is a good locator of the loss creation regions within the domain. So, contours of entropy generation rate are plotted on a meridional plane in Figure 15. Entropy is created through dissipation as well as heat transfer. Hence, both the sources were taken into account while calculating the entropy generation rate, although the contribution from the latter was negligible in this case. For each source, the entropy generation rate was calculated by summing the contributions from the mean flow field and the turbulence. The expressions used were [36]:

$$\dot{S}_{Dissipation} = \frac{\mu}{\overline{T}}\left[2\left\{\left(\frac{\partial \overline{V_x}}{\partial x}\right)^2 + \left(\frac{\partial \overline{V_y}}{\partial y}\right)^2 + \left(\frac{\partial \overline{V_z}}{\partial z}\right)^2\right\} + \left(\frac{\partial \overline{V_x}}{\partial y} + \frac{\partial \overline{V_y}}{\partial x}\right)^2 + \left(\frac{\partial \overline{V_x}}{\partial z} + \frac{\partial \overline{V_z}}{\partial x}\right)^2 + \left(\frac{\partial \overline{V_y}}{\partial z} + \frac{\partial \overline{V_z}}{\partial y}\right)^2\right] + \frac{\rho\varepsilon}{\overline{T}} \quad (7)$$

$$\dot{S}_{Heat\ Transfer} = \frac{\lambda_{eff}}{\overline{T}^2}\left[\left(\frac{\partial \overline{T}}{\partial x}\right)^2 + \left(\frac{\partial \overline{T}}{\partial y}\right)^2 + \left(\frac{\partial \overline{T}}{\partial z}\right)^2\right] \quad (8)$$

$$\dot{S} = \dot{S}_{Dissipation} + \dot{S}_{Heat\ Transfer} \quad (9)$$

where μ is the dynamic viscosity, ε is the turbulent dissipation rate, ϱ is the density, T is the static temperature and λ_{eff} is the effective thermal conductivity. The contours in Figure 15 show that the major source of entropy was the region of mixing between the re-entering leakage flow and the bulk flow (**A**). A significant amount of entropy was also seen to be created under the different seals due to the formation of jets by the leakage fluid (**B**). The shear flow interface between the inlet cavity vortex and the bulk flow was yet another source of entropy (**C**).

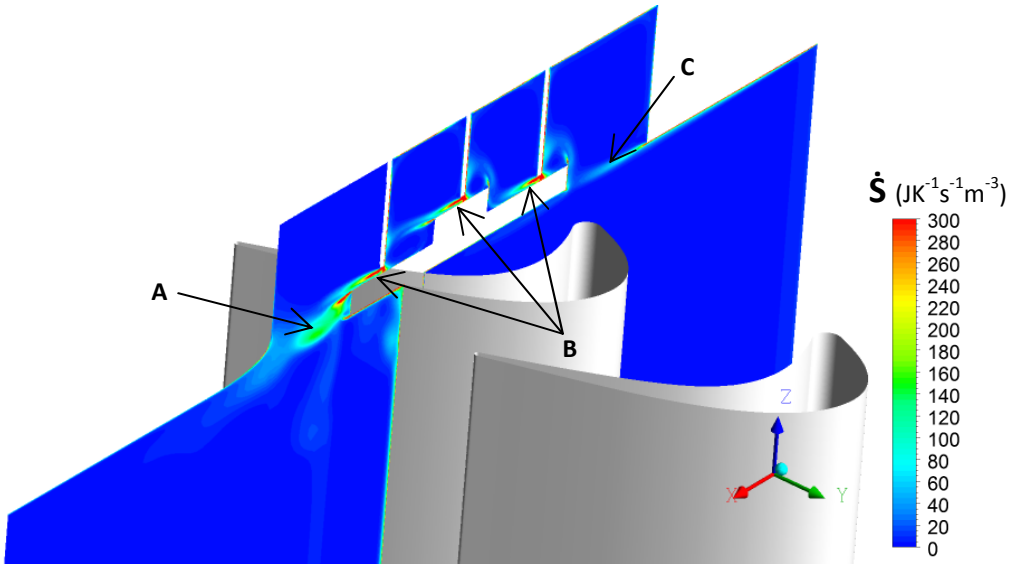

Figure 15, Baseline Case: Entropy Generation Rate on the Meridional Plane

In order to better understand the flow physics, the axial and tangential components of absolute velocity were studied on a meridional plane. They are shown in Figure 16. The following observations were made:

- The axial velocities of the jets under the seal teeth were nearly the same as that of the bulk flow. Because of this, the leakage jet from the last tooth was

seen to re-enter the bulk flow with a very similar axial velocity (**A**). After exiting from the last tooth, the leakage flow formed a free jet that was seen to quickly diffuse and turn towards the bulk flow.

- However, the behaviour of the tangential velocity was quite different. In the contours, the red colour implies a positive tangential velocity whereas the blue colour implies a negative tangential velocity. The bulk flow had a positive tangential velocity at the rotor inlet (**B**) which, after getting turned by the blade, became negative at the rotor exit (**C**). But the leakage fluid was seen to maintain a positive value throughout the leakage channel. In fact, the leakage jet under the last seal tooth still had approximately 50 percent of the tangential velocity at the rotor inlet. As a result, it had almost twice the tangential velocity of the exit flow and in the opposite direction. So there was a sharp variation in the magnitude and direction of the velocity when the leakage jet re-entered the bulk flow (**D**) which caused shear and the loss that was observed earlier.
- On a positive note, the tangential velocity of the leakage jet under the first tooth was approximately 7 percent higher than the shroud velocity (**E**). As the leakage fluid exerted a shear force on the shroud, it was acting to increase the rotor work up to some distance from the shroud leading edge.

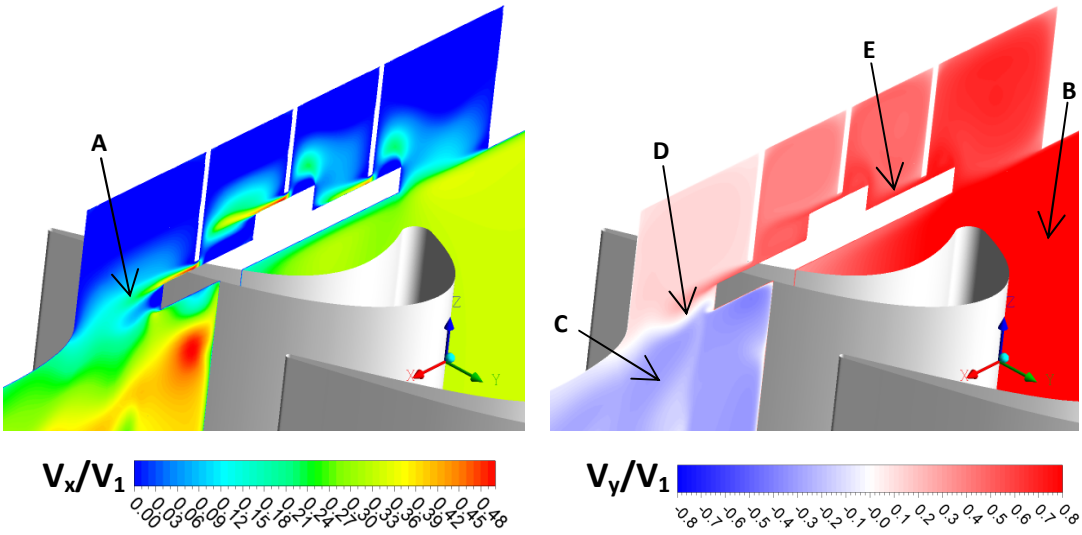

Figure 16, Baseline Case: Axial Velocity and Tangential Velocity on the Meridional Plane

As the interaction between the leakage flow and the bulk flow was three-dimensional in nature, streamlines were generated to observe the flow behaviour. In Figure 17, the white streamlines represent the fluid from the blade pressure side and the red streamlines represent the leakage flow over the shroud. Contours of entropy generation rate are also shown on a tangential-radial plane 30 percent axial chord behind the rotor. The location of the plane can be seen in the inset. The pressure side fluid showed ingress to the exit cavity and generated high entropy by mixing with the leakage flow (**A**). Due to this, the entropy generation was not uniform in the tangential direction. As a result of the pressure side flow ingress, the leakage flow also showed a non-uniform re-entry into the bulk flow. It was broken into jets that entered the bulk flow through the space next to the pressure side fluid (**B**).

Figure 18 shows streamlines representing the pressure side fluid (blue), the suction side horse shoe vortex (white) and the passage vortex (red). Helicity contours can also be seen. Helicity is defined as $\mathbf{H} = \boldsymbol{\omega}.\mathbf{u}$ where $\boldsymbol{\omega}$ and $\mathbf{u}$ are the vorticity and velocity vectors respectively. In a physical sense, helicity represents the 'degree of knottedness' of tangled vortex lines [37]. Its positive values indicate rotation in one sense (i.e. clockwise) and negative values indicate rotation in the other sense (i.e. anti-clockwise). A region of high negative helicity was observed where the pressure side fluid entered the exit cavity (**C**). It was because the tangential velocity of the bulk flow was very different from the leakage flow. So the high shear between the pressure side fluid and the leakage flow generated a strong vorticity. This feature of shroud leakage interaction is described in literature [14] as the "leakage vortex". The leakage vortex was seen to continue behind the rotor (**D**), but in a different direction to the secondary vortices. The interaction between these vortices modified the incidence downstream of the rotor as shown later in the axial progression of yaw angle (Figure 34). Not only would it increase the secondary loss of the downstream rows, the tangential variation in the yaw angle would produce high unsteadiness inside them.

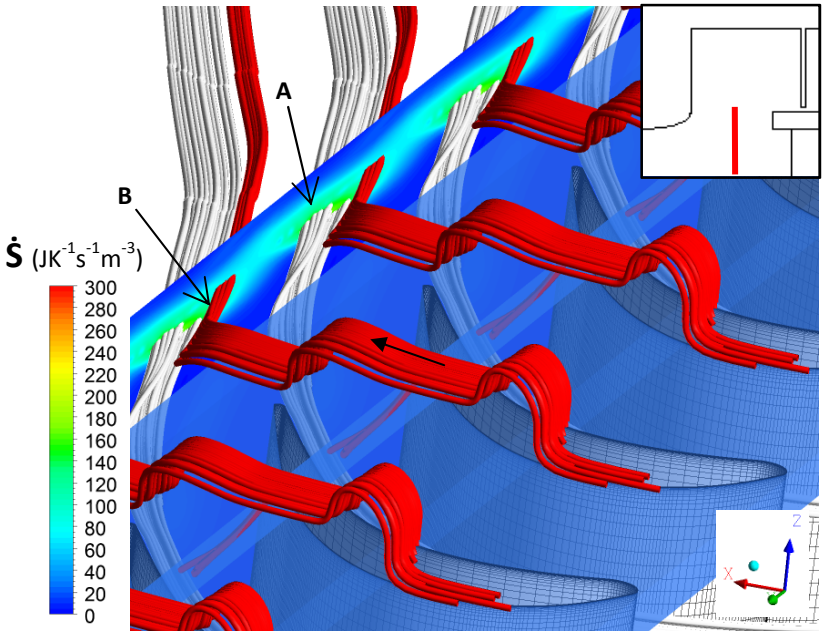

Figure 17, Baseline Case: Streamlines of Pressure Side Fluid and Leakage Flow

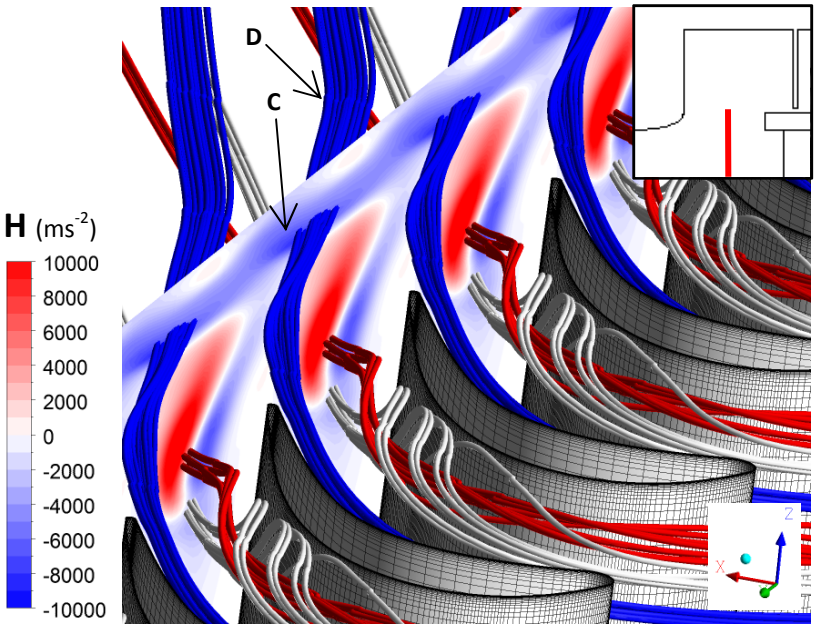

Figure 18, Baseline Case: Streamlines of Pressure Side Fluid and Secondary Flows

The flow features of the baseline case agreed well with the findings in the literature. So it was possible to apply the theory in order to understand the different flow phenomena observed in the baseline case.

6 Fluidic Jet Cases

Various fluidic jet configurations were investigated in order to select the best performing arrangement for the present study. The idea behind each configuration, its performance and the procedure for the selection of the best design are described in this chapter.

6.1 Basic Considerations

The fluidic jet was incorporated by modifying the baseline case. It was placed towards the shroud trailing edge near the exit cavity under the third tooth. This was done for two reasons:

- To turn the re-entering flow just before it met the bulk flow. If the fluidic jet were placed further upstream, much of its tangential component would be lost in going through the successive cavities before meeting the bulk flow.
- As seen in the baseline case flow analysis, the shear force exerted by the leakage fluid near the shroud leading edge acted to increase the rotor work. Placing the fluidic jet at the rear would not impact this favourable shroud shear.

So the last seal tooth was removed in order to accommodate the fluidic jet. The jet was constantly inclined at 45° to the horizontal for all configurations. The incline angle was selected from previous studies [4] which showed this to be the optimum angle for this application. For each configuration, care was taken to ensure that the inclusion of the fluidic jet did not hinder the axial and radial movements of the rotor, which occur during the turbine operation.

6.2 Jet Boundary Condition

A total pressure boundary condition was applied at the jet inlet. The jet pressure was increased in steps from zero up to the overblown condition, where some part of the jet fluid turned upstream and entered through the inlet cavity. In order to impart a tangential momentum to the leakage flow, the inflow velocity direction was set at the absolute rotor exit yaw angle (α_2) of 36.2°. This value was directly taken from the

baseline case results and was kept fixed for all the jet pressures. A study on the effect of changing the yaw angle would have increased the number of simulations significantly and so the rotor absolute value was considered a good place to begin with.

6.3 Fluidic Jet Configurations

Figure 19 shows the baseline case along with the four fluidic jet configurations *Ith*, *Blk*, *Noz* and *Uth* tested in the present study. Axial velocity contours on a meridional plane are also included to give an idea of the re-entering mass flow rate.

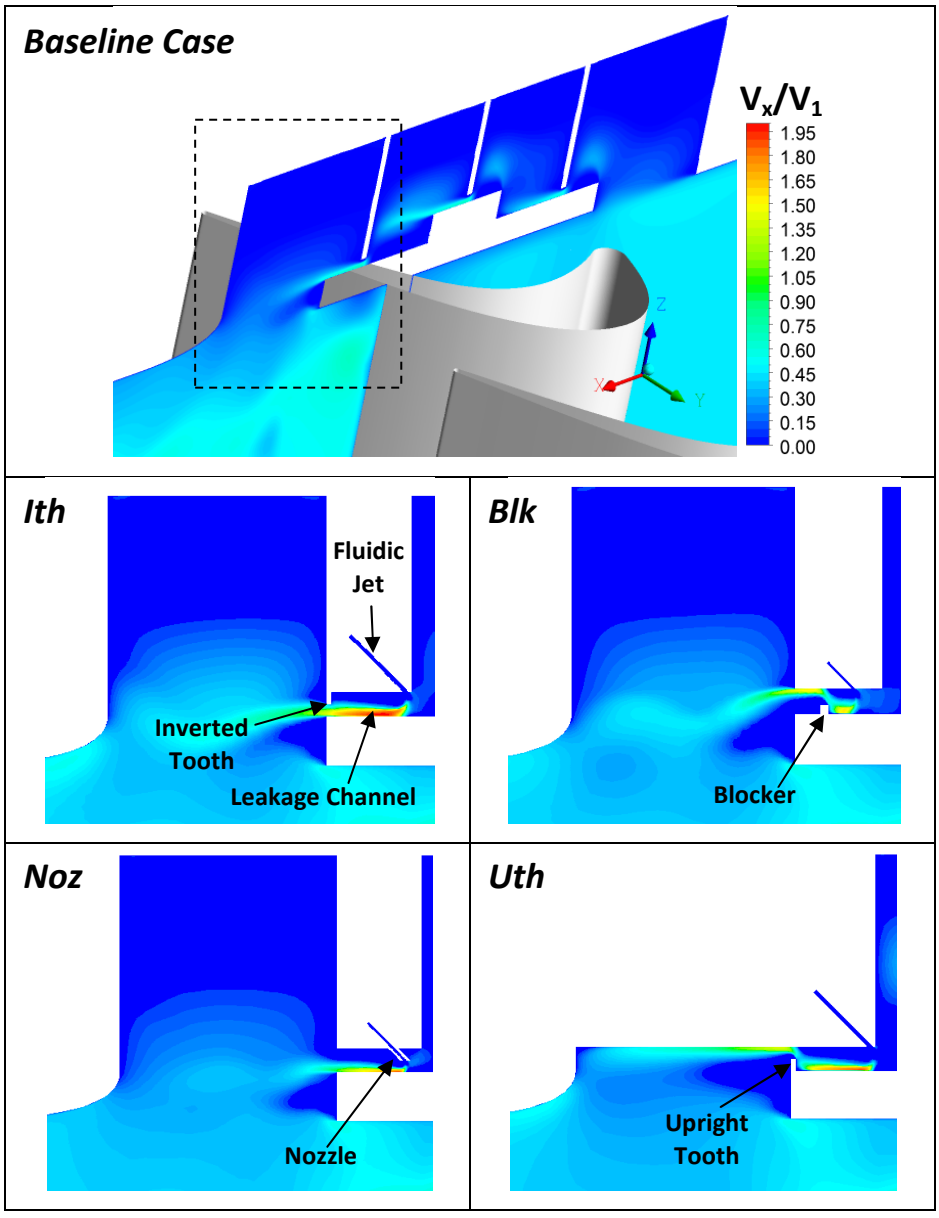

Figure 19, Fluidic Jet Configurations

6.3.1 Ith

Past research at Durham [4] had shown that if a fluidic jet was placed before the last seal clearance of a shrouded turbine, a reduction in the total re-entering mass flow was possible. So configuration *Ith* consisted of a fluidic jet followed by an inverted tooth. But the inverted tooth gave an easy path for the jet fluid to pass and so the kinetic energy of the jet got carried over under the tooth. As a result, the jet was not able to induce an effective blockage and a high jet inlet pressure was required to achieve an overblown condition. Such high pressure is not practical and so the overblown results were not included for this configuration. Also, the jet width, which was $1/6^{th}$ of the height of the leakage channel, was considered too large in terms of the jet mass flow rate it produced.

6.3.2 Blk

Because configuration *Ith* was not an effective design, in configuration *Blk*, the jet width was reduced to $1/10^{th}$ of the leakage channel height and a blocker was placed on the shroud just downstream of the jet. The blocker was effective in stopping the jet and preventing the kinetic energy carry over. However, due to a smaller jet width, a high jet pressure was required for it to be able to impinge the blocker and bring about a blockage. At low pressures, the jet simply turned halfway through the leakage channel and passed straight over the tooth.

6.3.3 Noz

In order to reduce the required jet inlet pressure, it was decided to incorporate a nozzle to support the jet up to half way across the leakage channel in configuration *Noz*. But the blocker had to be removed to avoid hindering the rotor axial movement during turbine operation. This time the jet was able to block more of the leakage flow at a lower supply pressure. In fact, the nozzle itself acted as a third tooth. Although there was no blocker, the jet was thin and so had ample space downstream of it to mix properly before re-entering the bulk flow without any kinetic energy carry-over.

6.3.4 Uth

In configuration *Uth*, the exit cavity was reduced and an upright tooth was placed at the shroud trailing edge. The nozzle had to be removed because it would have hindered the rotor axial movement. So, in order to reduce the required jet pressure, the jet width was increased back to 1/6th of the leakage channel height. As the tooth was upright, the jet was able to impinge it and thus give an effective blockage. Moreover, due to the reduced exit cavity, the re-entering fluid formed a wall jet that reduced its mixing rate with the bulk flow up to the rear edge of the exit cavity.

6.4 Performance Evaluation

The four designs were judged based on the two main rotor performance objectives: leakage reduction and mixing loss improvement. In addition, the overall total-to-total efficiency of the rotor was also taken into consideration.

6.4.1 Leakage Reduction

A fluidic jet that successfully blocks the leakage flow will reduce the mass flow entering through the first seal tooth (m_i). So its variation with the jet pressure ratio is shown in Figure 20(a) for the four different configurations, normalized by the rotor inlet mass flow rate (m_1). The negative values imply an overblown condition, i.e., the jet fluid entering the inlet cavity. As less flow leaves the bulk flow, more of it passes through the blade passage and the blade lift should increase. The blade lift is represented by the net tangential force on the blade (F_y) which is shown in Figure 20(b), normalized by F_y of the baseline case.

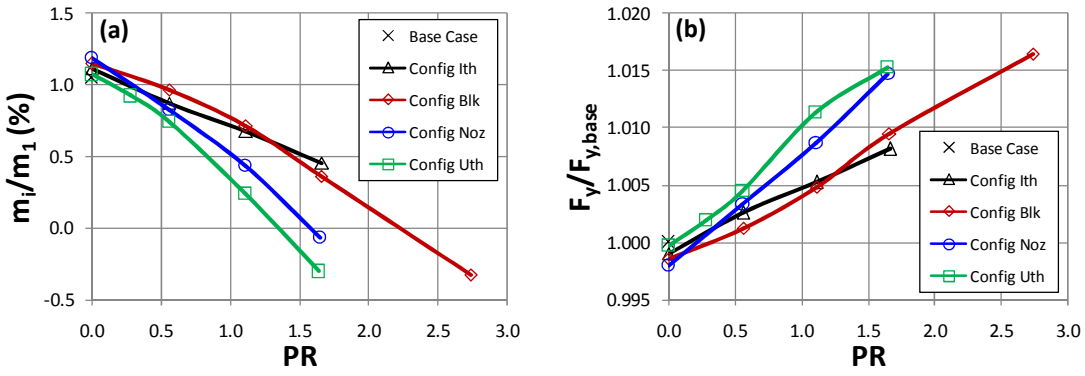

Figure 20, Fluidic Jet Configurations: Leakage Flow and Blade Tangential Force

Here the jet pressure ratio was defined as:

$$PR = \frac{p_{0j} - p_{s2}}{p_{01} - p_{s2}} \tag{10}$$

where P_{0j} is the jet inlet total pressure, P_{01} is the inlet total pressure and P_{s2} is the exit static pressure. At the zero jet pressure, the values were quite close to the baseline case. All the configurations showed a drop in the leakage flow with an increase in the jet pressure. This reduction was the highest for configuration *Uth* at all jet pressures, implying that it was the most successful in blocking the leakage flow. Configuration *Noz* was also quite effective, but showed a slightly lower leakage flow blockage compared to configuration *Uth*. Initially, the lowest performance was shown by configuration *Blk* as the jet was not able to impinge the blocker. However, as the jet pressure was sufficiently raised, it surpassed configuration *Ith*. But due to its thin jet, an overblown condition was achieved at a much higher supply pressure compared to configurations *Noz* and *Uth*.

A direct influence of the blockage was seen on the blade force, which increased by increasing the jet pressure. Configuration *Uth* produced the highest blade force, followed by configuration *Noz*. Again, configuration *Blk* crossed configuration *Ith* at a jet pressure ratio of approximately 1.2. It may be noted that, for configurations *Blk* and *Uth*, although the drop in the leakage mass flow was almost linear throughout, the force did not show a linear behaviour at the overblown condition. As shown later, this was because of enhanced secondary flows which reduced the turning through the rotor.

6.4.2 Mixing Loss Improvement

According to Denton's entropy model, the re-entry mixing loss of the fluidic jet configurations was dependent on two factors: the re-entering mass flow (leakage flow plus jet flow) and the tangential velocity difference between the re-entering flow and the bulk flow. So, both of them were investigated first in order to understand the mixing loss shown by the different configurations.

The general trend for the re-entering mass flow (m_e) was an initial rise followed by a drop as jet pressure was increased. Plots of re-entering mass flow rate (m_e) are presented in Figure 21, normalized by the rotor inlet mass flow rate (m_1). It may be noted that at the zero jet pressure, as the jet was not adding any fluid to the leakage flow, these values were the same as the leakage mass flow (m_i) in Figure 20(a). Configuration *Uth* was quite close to configuration *Blk*, which could be attributed to the blocker-type designs of both these configurations. In both of them, unless the jet impinged the blocker/tooth, it was simply adding fluid to the re-entering flow. The best performance in this case was that of configuration *Noz*. It showed only a negligible rise before the drop, meaning that, in this configuration, the fluidic jet was blocking at least as much leakage flow as it was adding to the re-entering flow.

For configuration *Ith*, the re-entering mass flow kept increasing with the jet pressure. This was because the kinetic energy carry over under the tooth did not allow the jet to mix before its re-entry. There is a pressure recovery associated with this mixing, as shown by Curtis et al. [2] in their measurements of a fluidic jet. As this recovery could not happen, the jet saw a lower pressure downstream of it and continued to accelerate towards the exit cavity. Configurations *Blk* and *Noz* were able to give a reduction compared to the baseline case, although only at the overblown condition. This did not happen for configuration *Uth* even when it was overblown, which could be because of its higher jet width that was sending in more mass flow.

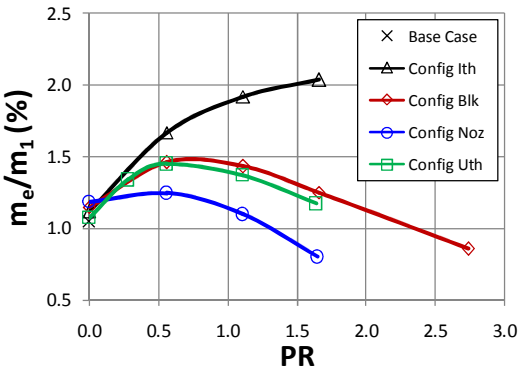

Figure 21, Fluidic Jet Configurations: Re-Entering Mass Flow Rate

The fluidic jet was able to turn the re-entering fluid towards the bulk flow in all the configurations. Figure 22 shows the tangential velocities for the baseline case along

with configurations *Noz* and *Uth* at the jet pressure ratio of 1.1. The amount of turning increased with the jet pressure: A higher jet pressure implied a higher jet tangential momentum and, following the law of conservation of momentum in the tangential direction, the re-entering flow was turned more. This had an interesting implication on the exit cavity vortex. While in the baseline case, the exit cavity vortex travelled against the bulk flow, its direction was reversed for the fluidic jet cases. The vortex also travelled faster as jet pressure was raised, due to an increase in the tangential velocity of the re-entering flow. In configurations *Blk* and *Noz*, due to the smaller width of the jet, it could not turn the re-entering flow sufficiently even at high jet pressures. As a result, a considerable difference still existed between the tangential velocities of the cavity vortex and the bulk flow. In configuration *Ith*, although the wider jet had a higher tangential momentum, the re-entering flow lost much of its tangential component as it mixed inside the large exit cavity space. So the exit cavity vortex was still slower compared to the bulk flow.

However, configuration *Uth* did not have such a vortex because of its reduced exit cavity. Since the re-entering fluid formed a wall jet, it was able to maintain its tangential momentum all the way up to the rear edge of the cavity. A uniform distribution of tangential velocity was observed throughout the exit cavity in this case.

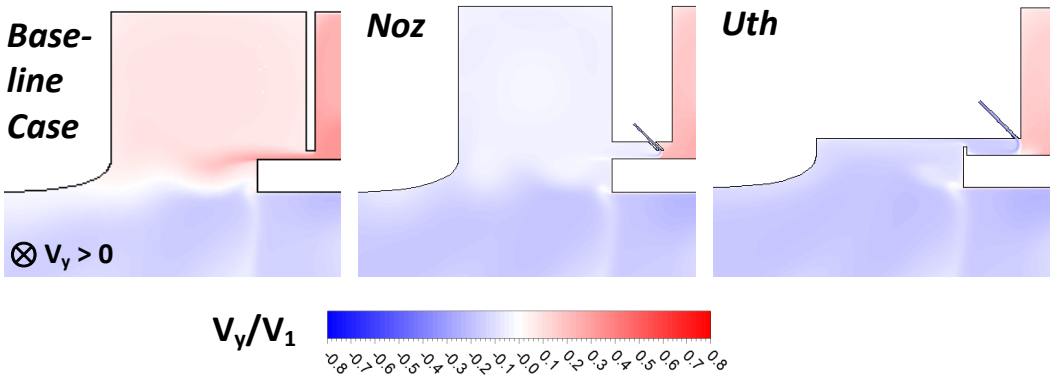

Figure 22, Fluidic Jet Configurations: Tangential Velocity on the Meridional Plane near the Exit Cavity

Now that the two factors, namely the mass flow and turning of the re-entering fluid, have been discussed for the different configurations, the mixing loss shown by them

can be understood. The relative total pressure loss coefficient is shown in Figure 23 for the baseline case and the configurations *Noz* and *Uth* at the jet pressure ratio of 1.1. Considering only the re-entering mass flow rate, configuration *Noz* seemed to be the most promising. But when its tangential velocity was investigated, it was seen that a shear still existed between the slow moving cavity vortex and the high speed bulk flow and this led to a considerable mixing loss generation. A similar phenomenon was observed in configurations *Ith* and *Blk*; although the shear was lower for configuration A due to a faster moving cavity vortex. Furthermore, in all these configurations, the loss layer showed a wavy boundary structure because of a higher penetration of the cavity fluid towards the wake suction side.

On the other hand, the reduction of the exit cavity in configuration *Uth* produced favourable results. As the re-entering wall jet did not lose its tangential momentum before it met the bulk flow, there was a significant reduction in the mixing loss. The downstream flow was also more uniform in that the wavy loss pattern was not present.

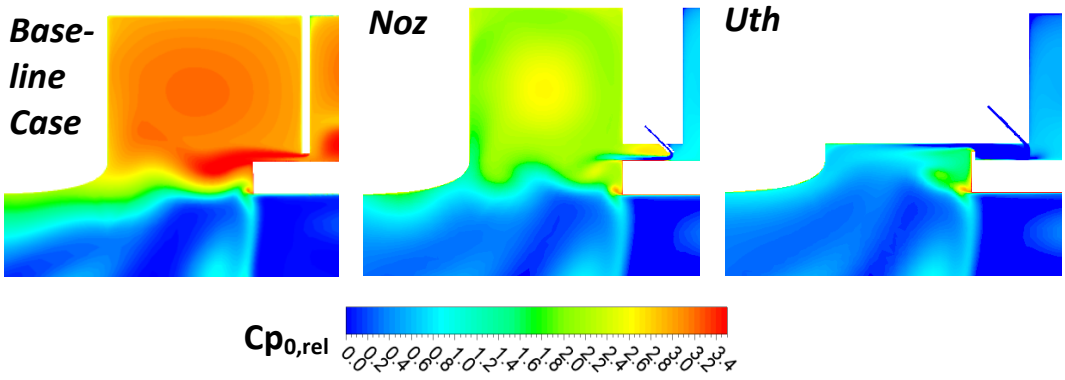

Figure 23, Fluidic Jet Configurations: Loss on the Meridional Plane near the Exit Cavity

The fluidic jet was found to have an impact on the rotor secondary loss. As more leakage flow was blocked by the fluidic jet, it was forced to re-enter the bulk flow through the inlet cavity, leading to a thickening of the boundary layer at the shroud leading edge. This can be seen in Figure 24 which features a thicker high loss region at the shroud leading edge for configuration *Uth* at the jet pressure ratio of 1.1, compared to the baseline case. As a result, the secondary flows were slightly

enhanced as jet pressure was raised as shown in Figure 35 later on. It was only at the overblown condition that this enhancement was significant. This was because, in this condition, the fluid was being added to the inlet cavity rather than being removed from it. However, the wake loss showed negligible variation with the jet pressure. So the overall loss at the rotor exit was, in fact, a trade-off between the mixing and the secondary losses.

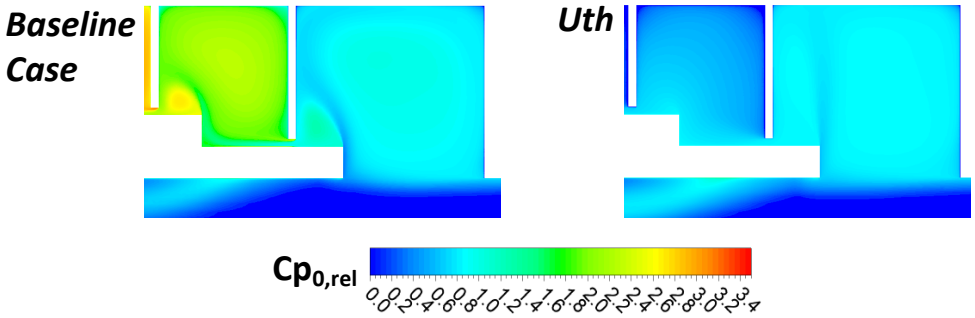

Figure 24, Fluidic Jet Configurations: Loss on the Meridional Plane near the Inlet Cavity

In order to compare the overall loss for the different configurations, mass-averaged values of the relative total pressure loss coefficient were calculated one axial chord behind the rotor trailing edge. This location, referred to as $2.0C_x$, was well behind the exit cavity and so downstream of the leakage interaction. The variation of the mass-averaged loss is presented in Figure 25.

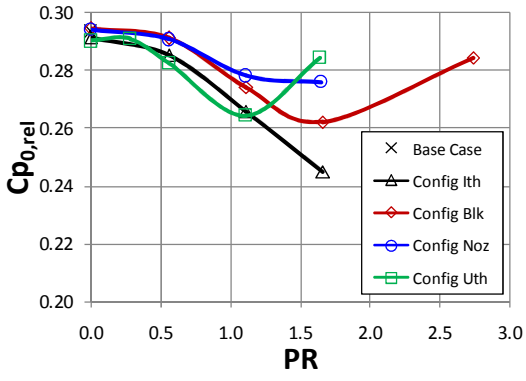

Figure 25, Fluidic Jet Configurations: Mass-averaged Loss at $2.0C_x$

The loss values for the fluidic jet configurations were very similar to the baseline case at the zero jet pressure. This could be attributed to their matching leakage levels seen

in Figure 20. Up to the jet pressure ratio of 1.1, the leakage loss reduction dominated the secondary loss enhancement and so the lowest loss was shown by configuration *Uth*. But at the overblown condition, the secondary loss took over and a rise in the loss coefficient was observed for configurations *Blk* and *Uth*. Configuration *Noz* did not show such a rise because, as can be seen in Figure 20(a), it did not overblow the seal as much as the other configurations. Interestingly, configuration *Ith* showed a low loss and followed closely behind configuration *Uth*. But the reason was that, due to its less effective blockage, it simply pumped energy into the rotor exit flow and did not enhance the secondary flows arising from the rotor leading edge as much.

6.4.3 Overall Efficiency

In an industrial turbine, the supply pressure for the fluidic jet would have to be obtained from somewhere within the thermodynamic cycle. So it was considered useful to have an idea of the overall efficiency of the fluidic jet configuration that accounted for the energy given to the jet. The overall efficiency was calculated as:

$$\eta\,(\%) = \left(\frac{F_y \times U}{\dot{m}_1 c_p T_{01}\left[1 - \left(\frac{p_{02}}{p_{01}}\right)^{\frac{\gamma-1}{\gamma}}\right] + \dot{m}_j c_p T_{0j}\left[1 - \left(\frac{p_{02}}{p_{0j}}\right)^{\frac{\gamma-1}{\gamma}}\right]} \right) \times 100 \qquad (11)$$

where F_y is the blade/shroud tangential force, U is the blade velocity, $\dot{m}_1$ is the inlet mass flow rate, $\dot{m}_j$ is the jet inlet mass flow rate, c_p is the specific heat of air, T_{01} is the inlet total temperature, T_{0j} is the jet inlet total temperature, P_{01} is the inlet total pressure, P_{0j} is the jet inlet total pressure, P_{02} is the exit total pressure and γ is the ratio of specific heats. Here, the numerator represented the power output from the rotor. The first term in the denominator was the ideal work that could be extracted if the inlet air were expanded to the outlet total pressure. The same was represented for the jet air by the second term. Hence, this efficiency expression accounted for the extra energy put into the system and was a measure of the overall performance of the fluidic jet configurations. Before looking at the efficiency data, it is important to understand how the various terms in the efficiency expression changed as the jet pressure was raised:

- Due to an increase in the blade force with the jet pressure, the numerator increased.
- The first term in the denominator had two variables, the inlet total pressure and the exit total pressure. The rotor inlet total pressure was seen to increase with the jet pressure. This was because as the mass flow through the blade passage increases, there is a larger pressure drop across the blade [1]. The exit total pressure also increased due to a combined effect of the inlet total pressure rise and reduced mixing loss. But overall, this term became larger.
- The second term in the denominator was dominated by the jet mass flow rate and the jet total pressure and so the jet pressure increased this term also.

Clearly, the overall efficiency was a trade-off between the numerator and the denominator. Figure 26 presents the efficiency plots. For all configurations, the zero jet pressure efficiencies were calculated in the same way as the baseline case, without the jet term in the denominator. As their blade lifts were quite similar (Figure 20(b)), their efficiencies were very close to the baseline case. The efficiency values showed small changes up to the jet pressure ratio of 0.6, which was followed by a rapid drop in efficiency with increasing jet pressure ratio. Configuration *Noz* showed a slight increase in the efficiency before the drop, but the baseline case still showed the highest efficiency.

From this trend, it was concluded that there existed a configuration dependent critical jet pressure up to which the increase in the rotor work (numerator term) raised the efficiency. Once this critical pressure was crossed, the energy supplied to the jet and the increased blade pressure drop (denominator terms) started to dominate the efficiency expression. The exact value of the critical jet pressure value would need to be determined by running more closely spaced jet pressure ratio tests for each configuration separately over the range $0 \leq PR \leq 0.6$.

Previously, configuration *Uth* had been shown to produce the highest blockage. So it was decided that for configuration *Uth* the jet pressure ratio of 0.6 had already crossed the critical jet pressure value. Hence, an additional test was performed with a jet pressure ratio of 0.3. The result confirmed the expectations and an increase in the

efficiency compared to the zero jet pressure case was observed. In fact, configuration *Uth* showed the highest efficiency among all the four configurations. It was also the only configuration to show a higher efficiency than the baseline case. However, as this efficiency gain was very small, it must be kept in mind that such small computationally predicted changes in efficiency are seldom reliable and should be interpreted with caution.

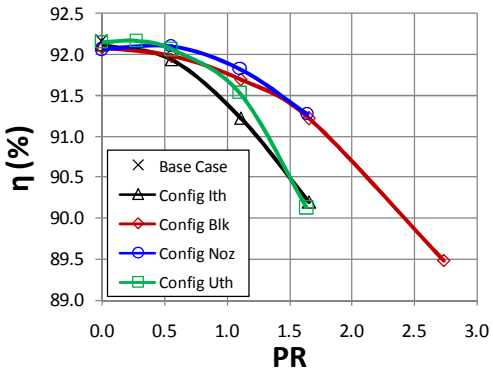

Figure 26, Fluidic Jet Configurations: Overall Total-to-Total Efficiency

6.5 Final Configuration

With the performance analysis of the fluidic jet configurations complete, it was possible to select the best performing configuration. The analysis revealed that configuration *Uth* gave the best results in terms of all the performance criteria, i.e. leakage reduction, mixing loss improvement and the overall efficiency. So it was selected as the final configuration for further study in the following chapter.

7 Results Analysis

This chapter seeks to analyze the selected configuration *Uth*, hereafter referred to as the 'fluidic jet case', and to compare its results with the baseline case. It begins with a flow field description of the fluidic jet case. Then a comparison is made between the pitch-averaged results of the baseline case and the fluidic jet case on axially progressing planes at the rotor exit. Following this, the impact of raising the fluidic jet pressure is investigated in terms of flow variables and loss breakdown one axial chord downstream of the rotor trailing edge. Finally, the effect on other turbine aspects such as work coefficient and flow coefficient is discussed.

7.1 Fluidic Jet Case Flow Features

The flow field analysis for the fluidic jet case was performed at the jet pressure ratio of 1.1. This particular jet pressure was chosen because it gave the best performance in terms of the rotor exit loss (Figure 25). Figure 27 shows the relative total pressure loss coefficient on a meridional plane for the baseline case and the fluidic jet case.

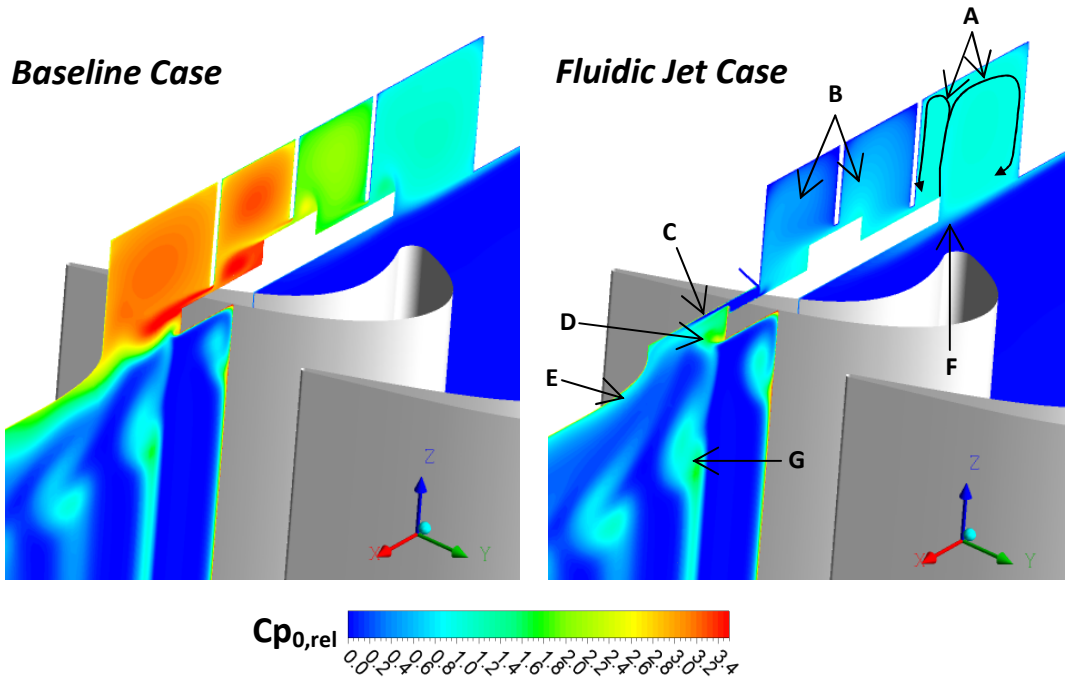

Figure 27, Fluidic Jet Impact: Loss on the Meridional Plane

The following observations were made:

- Like the baseline case, some of the incoming flow left the bulk flow and entered the inlet cavity. However, this time there was a formation of two large vortices inside the inlet cavity (**A**). It was because of the reduced leakage flow due to the blockage effect of the fluidic jet. The fluid entering the inlet cavity was pushed up after which it split into a large vortex and a small vortex. As shown in Figure 28, it was primarily the fluid from the larger vortex that re-entered the bulk flow, and the fluid from the smaller vortex fluid that passed under the first seal tooth.

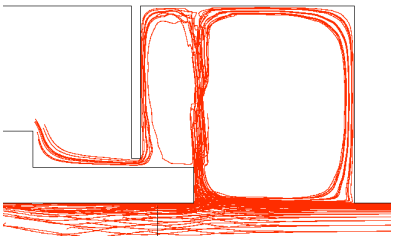

Figure 28, Fluidic Jet Case: Streamlines at the Inlet Cavity

- The loss level inside the inlet cavity was close to the baseline case. But it was much lower in the middle cavities (**B**). The reason for this was that as the fluidic jet had reduced the leakage mass flow, the jets under the seal teeth had lower velocities. So their mixing inside the downstream cavity space was reduced, leading to a smaller loss creation.
- The fluidic jet turned the leakage flow, and the two fluids entered the exit cavity together as the re-entering flow (**C**). Due to the reduced exit cavity, there was no space for the formation of a large cavity vortex here. The re-entering flow simply formed a wall jet, travelled towards the rear of the cavity and entered the bulk flow. Some of the bulk flow from the blade passage entered the space under the re-entering wall jet. A part of it continued downstream and mixed with the wall jet while the other part turned upstream and formed a small vortex sticking to the shroud trailing edge (**D**). The vortex was also seen to entrap some of the fluid from the re-entering wall jet. Significant shear was generated as this vortex interacted with the wall jet and this was the reason for the high loss seen in this region. It may be noted that a similar vortex was seen in the baseline case. But in this

case it was bigger because the wall jet and the upright tooth gave it more space to occupy.

- Downstream of the exit cavity, there was a slight increase in the loss towards the casing (**E**), which was due to the interaction between the re-entering flow and the bulk flow. But this loss region was significantly thinner compared to the thick high loss layer observed in the baseline case. This was the beneficial effect of the fluidic jet which had turned the re-entering flow towards the bulk flow and improved the mixing between them as a result. Furthermore, the fluidic jet itself was supplied with kinetic energy by its tangential and axial velocities which was carried over to the rotor exit.
- Since most of the inlet cavity fluid was recirculating rather than leaving through the first seal gap, the flow mixing between the inlet cavity vortex and the bulk flow was slightly enhanced. This led to a higher shear at their interface and so a thicker boundary layer was observed at the shroud leading edge (**F**). The result was a small increase in the strength of secondary flows compared to the baseline case (**G**). Due to the increased mass flow through the blade passage, the blade trailing edge wakes were slightly thinner and featured a greater mean velocity gradient than the baseline case.

The entropy generation rates for the baseline case and the fluidic jet case are compared in Figure 29. The fluidic jet case showed significant differences: The high entropy generation observed in the re-entry mixing region of the baseline case disappeared, confirming the positive impact of the fluidic jet in this flow area (**A**). In addition, the entropy production under the seal teeth was removed due to the weakened leakage jets (**B**). However, there was severe entropy generation just downstream of the fluidic jet. The reasons for this were: First, there was high shear between the fluidic jet and the leakage flow, since they had very different velocities. Second, the tangential component of the fluidic jet opposed the shroud motion which created additional shear. Third, a small but intense vortex was formed between the fluidic jet and the upright tooth (**C**). Fourth, the high energy wall jet was a major source of entropy in itself (**D**). The enhanced secondary flows showed a slightly higher entropy generation compared to the baseline case (**E**).

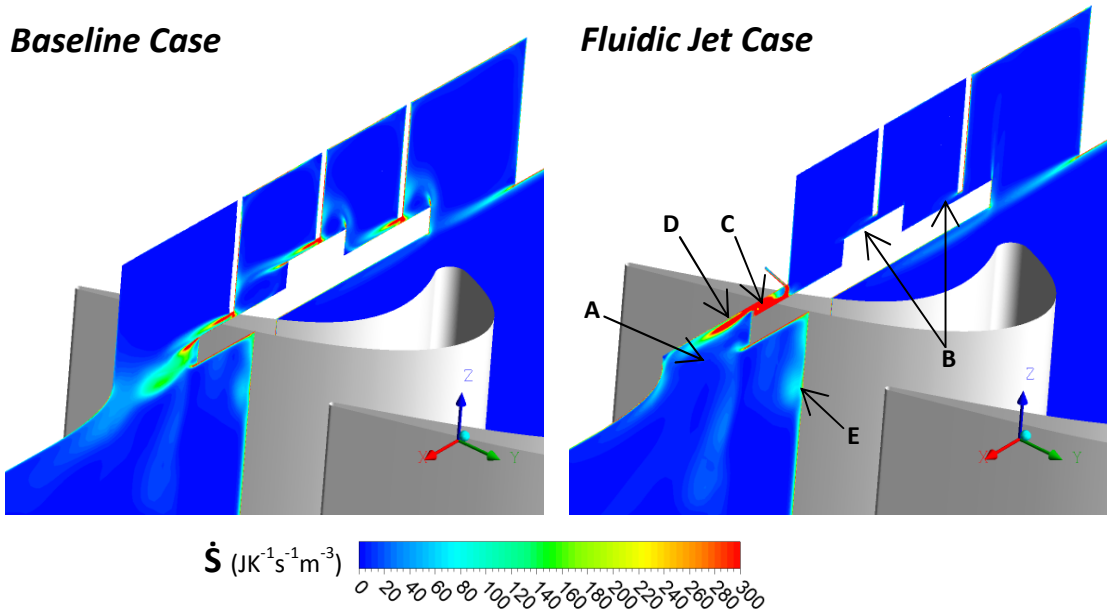

Figure 29, Fluidic Jet Impact: Entropy Generation Rate on the Meridional Plane

Finally, streamlines were generated to study the physics of the interaction between the leakage flow and the bulk flow in more detail. The streamlines for the pressure side fluid (white) and the leakage flow (red) are shown in Figure 30 along with contours of entropy generation rate on a tangential-radial plane 30 percent axial chord behind the rotor. For the fluidic jet case, the leakage flow was seen to be turned tangentially towards the bulk flow due to the fluidic jet impact. In fact, compared to the baseline case, the flow through the last seal tooth was found to be turned by approximately 58° in the tangential direction towards the bulk flow. The pressure side fluid showed a tendency of ingress to the exit cavity (**A**), as observed for the baseline case. This ingress broke the re-entering flow sheet into distinct jets (**B**). A high entropy generation was seen inside these jets but there was no variation in the tangential direction (**C**).

Figure 31 illustrates the streamlines representing the pressure side fluid (blue), the passage vortex (red) and the suction side horse shoe vortex (white). Helicity field is also presented. For the fluidic jet case, a uniform region of high negative helicity was seen where the pressure side bulk flow interacted with the re-entering wall jet (**D**). The helicity observed in this region was higher than the baseline case. Since helicity is the dot product of the vorticity and the velocity vectors, this high helicity was

caused by the tangential velocity difference of the interacting flows and the high velocity of the re-entering jet. But this was not a bad scenario, as shown later in the pitch-averaged results, because it was this phenomenon that brought the yaw angle near the casing close to the mid span value at the rotor exit. Moreover, the uniform helicity indicated that the fluidic jet case was less likely to induce tangential non-uniformity in the downstream rows compared to the baseline case. The secondary vortices moved radially towards the blade mid-span, as is usually observed with their enhancement.

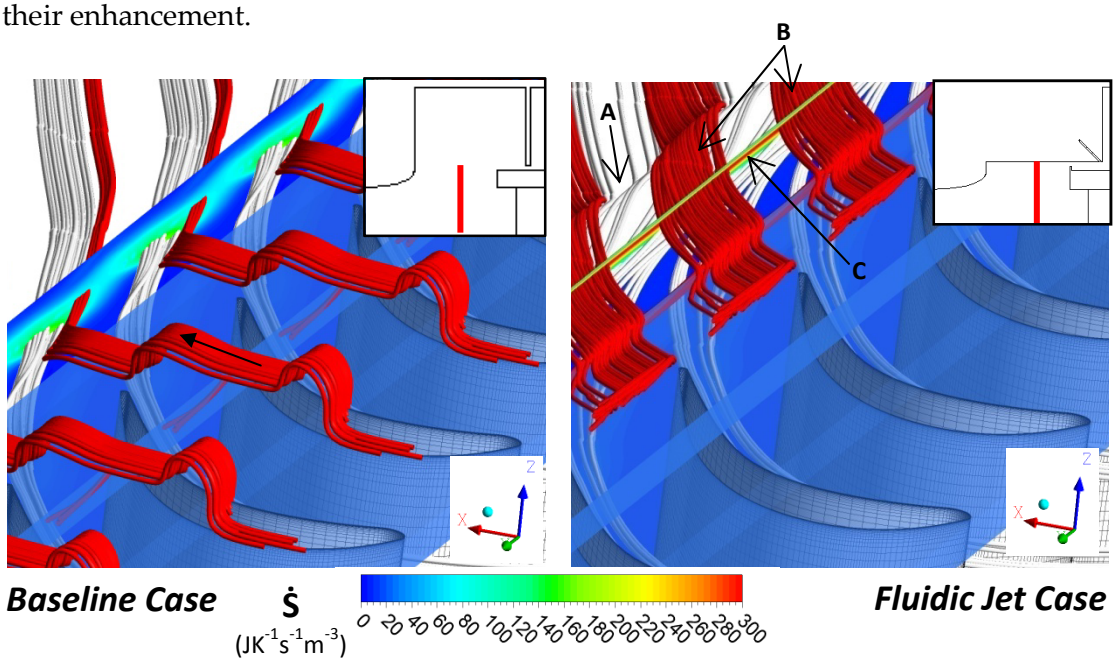

Figure 30, Fluidic Jet Impact: Streamlines of Pressure Side Fluid and Leakage Flow

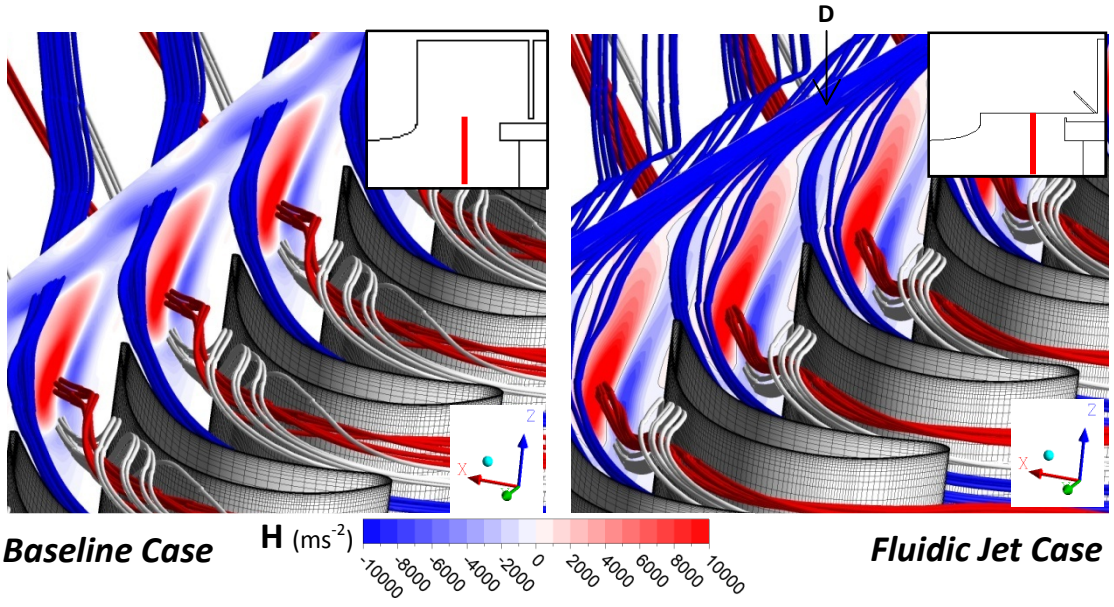

Figure 31, Fluidic Jet Impact: Streamlines of Pressure Side Fluid and Secondary Flows

7.2 Axial Progression Comparison

In this section, the flow behaviour is compared between the baseline case and the fluidic jet case on axially progressing planes behind the rotor. The axially progressing planes were named after their distance from the rotor leading edge. For instance, the $1.1C_x$ plane was 110 percent of the axial chord (C_x) behind the rotor leading edge, or 10 percent of the axial chord behind the rotor trailing edge, and so on. The locations of these planes relative to the rotor are shown in Figure 32. Streamlines are also shown (orange = leakage flow; green = bulk flow) to highlight the plane location with respect to the leakage – bulk flow interaction.

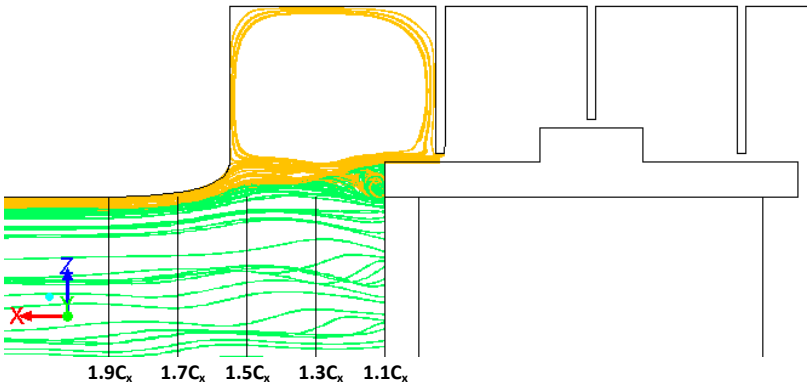

Figure 32, Axially Progressing Plane Locations

7.2.1 Loss Coefficient

Pitch-averaged plots of the relative total pressure loss coefficient on axially progressing planes are presented in Figure 33.

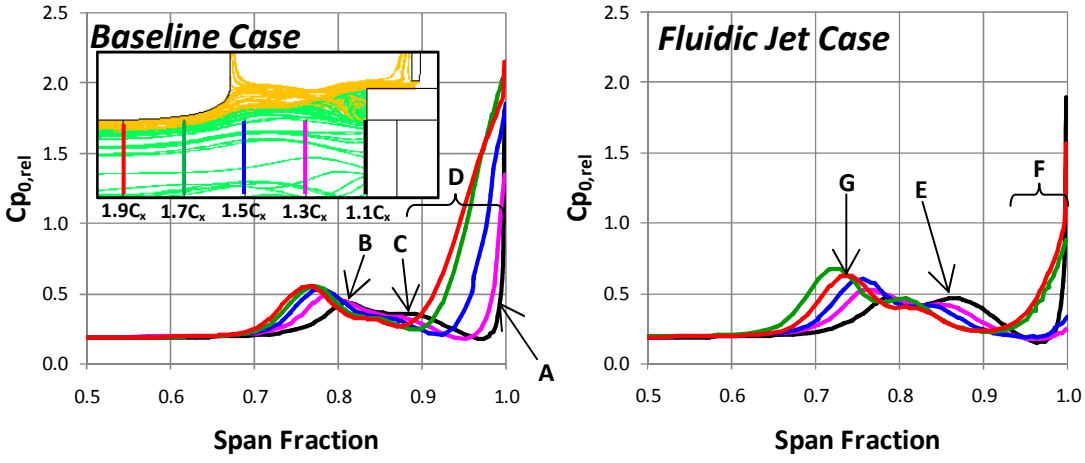

Figure 33, Axial Progression of Pitch-averaged Loss

For the baseline case, as $1.1C_x$ was at the upstream edge of the exit cavity, it did not contain any leakage effects. The loss increase near the shroud (span 1.0) was only due to the boundary layer (**A**) and the secondary flow loss. Two distinct bumps representing the suction side horseshoe vortex (**B**) and the passage vortex (**C**) were identified. Mixing losses started appearing at $1.3C_x$ towards the cavity (span 1.0). It was because this was the location where the leakage jet, after passing over the shroud trailing edge vortex, started to mix directly with the bulk flow. Then there was a sudden loss increase from $1.3C_x$ through $1.5C_x$ to $1.7C_x$. This was due to the interaction between the exit cavity vortex and the bulk flow. After this, the loss continued to show some variation from $1.7C_x$ to $1.9C_x$, indicating that the mixing was still incomplete. The thickness of the leakage loss region was also seen to increase continuously from $1.3C_x$, and reached nearly 12 percent of the blade span at $1.9C_x$ (**D**). It is worth noting here that the aspect ratio of the present blade was 2:1, whereas the aspect ratio may be as low as 1:1 in HP turbine stages. So, in that case, the present leakage loss layer would have covered a significant portion of the rotor exit area.

The fluidic jet case had a very similar loss behavior at $1.1C_x$, with the secondary flows and the boundary layer effects visible. There was a small increase in the secondary loss, especially for the passage vortex (**E**). The secondary flows were also shifted slightly towards the mid-span which is usually seen with an increase in their strength. It may be noted that, in this case, the re-entering flow was a wall jet which entered the bulk flow at the rear edge of the exit cavity. So the leakage loss appeared only at $1.7C_x$ because it was downstream of the exit cavity. However, due to the alignment in the tangential direction between the bulk flow and the jet, and the high energy of the re-entering flow, the added loss was significantly lower than in the baseline case. As a result, the thickness of the leakage loss layer at $1.9C_x$ was reduced to approximately 7 percent of the blade span (**F**). This was almost half of the thickness that was seen in the baseline case and showed the beneficial effect of the fluidic jet. A reduction in the mixing loss would effectively mean an increase in the useful energy of the rotor exit fluid. This extra energy would be available to the downstream blade rows and would increase the turbine work output. Another notable point at $1.9C_x$ was that, compared to the baseline case, the suction side

horseshoe vortex had shifted by nearly 5 percent of the blade span towards the blade mid-span (**G**).

7.2.2 Yaw Angle

The rotor exit yaw angle is an important flow parameter because it determines the incidence seen by the downstream blade row. It should be kept as close to the design angle as possible, especially towards the casing. This is because, if the yaw angle deviates too much from the design value near the casing, this can lead to enhanced secondary flows in the downstream row. Axial progressions of the pitch-averaged rotor exit yaw angle are shown in Figure 34 for the baseline case and the fluidic jet case.

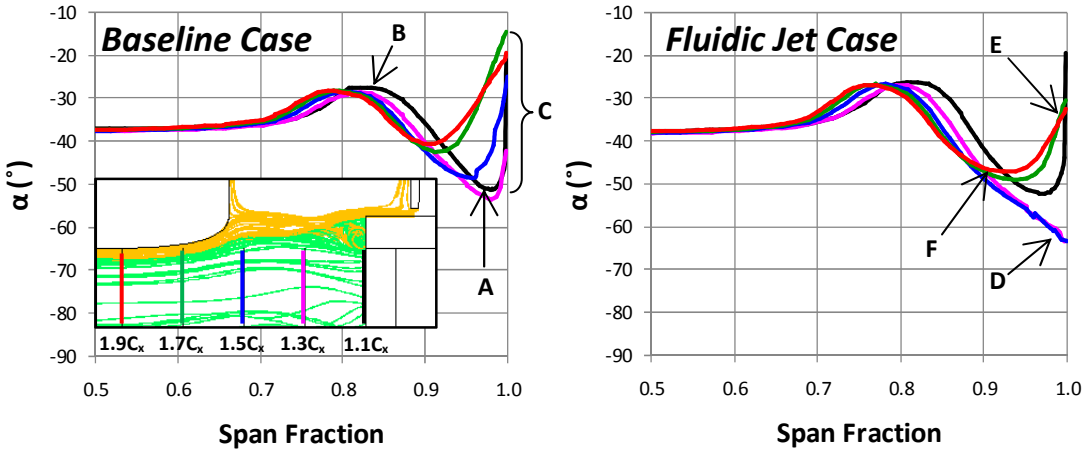

Figure 34, Axial Progression of Pitch-averaged Yaw Angle

The baseline case showed typical secondary flow behaviour at $1.1C_x$ [38], with an overturning near the shroud (**A**) and an underturning away from it (**B**). As the axial progression of loss had revealed that the major leakage interaction started at $1.5C_x$, there was not much variation in the yaw angle at $1.3C_x$. From $1.3C_x$ to $1.7C_x$, a substantial reduction in the yaw angle was noticed towards the cavity (span 1.0). This was because the leakage flow had a tangential velocity of an opposite sign. So it acted to reduce the turning of the bulk flow in the interaction region. The result was that the flow conditions near the cavity changed from a 15° overturning at $1.1C_x$ to a 20° underturning at $1.7C_x$ (**C**). An underturning towards the casing would create a negative incidence on the downstream row and thus enhance its secondary flows.

For the fluidic jet case, an overturning of 20° was seen towards the cavity at $1.3C_x$ and $1.5C_x$ (**D**). This could be attributed to the high energy bulk flow entering the exit cavity and moving in an almost tangential direction inside the cavity. However, at $1.7C_x$, the yaw angle showed a significant reduction in underturning near the cavity (**E**). It was due to the fact that, here, the flow near the casing consisted only of the re-entering wall jet. Since the fluidic jet was supplied at the same yaw angle as the bulk flow, the yaw angle of the re-entering jet matched the mid-span value very closely. This would help to reduce the secondary loss in the downstream row. At $1.9C_x$, an increase in the overturning of 8° due to the enhanced passage vortex was noticed (**F**).

7.3 Fluidic Jet Impact

7.3.1 Pitch-averaged Results

Based on the understanding gained from the analysis in the last section, it is now possible to look at the impact of raising the fluidic jet pressure on the rotor exit flow field. Pitch averaging was performed at $2.0C_x$ location, i.e., one axial chord behind the rotor trailing edge. Figure 35 presents these results for the baseline case and for the different jet pressure ratios of the fluidic jet case. An extra case of a flat wall without cavities, and so no leakage, had also been computed as shown in Figure 35. These results are also included for comparison.

The first notable feature of these results was that the zero jet pressure results were exactly superimposed on the baseline case results. It is worth remembering here that, for the zero jet pressure case, the re-entering flow was a wall jet whereas it was a free jet for the baseline case. So this close match of results showed that as long as the leakage mass flow and direction were kept constant, the manner of the leakage interaction might not impact the mixed out results after the interaction.

As the fluidic jet pressure was increased, there was a reduction in the relative total pressure loss coefficient near the casing. This was because of an increasingly higher turning and energy of the re-entering flow due to the fluidic jet. Initially, the pressure ratio of 0.6 caused only a small improvement. But at the 1.1 pressure ratio, there was a substantial reduction in the loss towards the casing. Although the suction side

vortex core showed a higher loss, this increment was only about 10 percent. Raising the jet pressure further to 1.6 (overblown condition) did not improve the leakage loss much, but increased the secondary loss considerably. It was because, at the overblown condition, instead of fluid being removed from the inlet cavity by leakage, the fluidic jet was adding fluid to it. This worsened the interaction between the inlet cavity fluid and the bulk flow and thus enhanced the secondary flows significantly. This was also the reason for the sudden jump in the mass-averaged loss coefficient that was observed in Figure 25 for this pressure ratio. The flat wall result revealed a higher secondary loss compared to the baseline case. It confirmed that the removal of the boundary layer by the inlet cavity had weakened the secondary flows in the baseline case.

The pressure coefficient (Cp) was defined as follows:

$$\mathrm{Cp} = \frac{\mathrm{P_s} - \mathrm{P_{s1}}}{\mathrm{P_{01}} - \mathrm{P_{s1}}} \tag{12}$$

The pitch-averaged results showed a drop in the pressure coefficient with an increase in the fluidic jet pressure. This could be understood from the above expression for the pressure coefficient. As the jet pressure was raised, the mass flow and so the pressure drop across the rotor increased. Since the inlet dynamic pressure (P_{d1}) and the exit static pressure (P_s) were fixed by the boundary conditions of the simulation, the only way for the pressure drop to increase was through an increase in the inlet static pressure (P_{s1}). So, by definition, a drop in the pressure coefficient resulted. Hence, a lower pressure coefficient at the rotor exit pointed to a higher inlet static pressure rather than a lower exit static pressure.

At zero jet pressure, due to the leakage interaction, the yaw angle showed an underturning of approximately 10° near the casing. Raising the jet pressure ratio to 1.1 improved the yaw angle by 12° in this region, thus making it only 3° different from the mid-span value. In fact, this value was even better than the flat wall case which had an overturned flow at the casing on account of secondary flows. But at the overblown condition, a flow overturning was observed near the casing. This yaw

angle behaviour can be understood from its definition. The absolute yaw angle was defined as:

$$\beta = \tan^{-1}\left(\frac{V_y}{V_x}\right) \tag{13}$$

So the yaw angle depended on the axial and the tangential components of velocity. As the jet pressure was raised, the axial velocity increased by approximately 5 percent near the casing. It was because the jet was adding extra fluid and so increasing the mass flow in this region. However, the tangential velocity showed up to 15 percent increase in the same region. This was due to the tangential momentum imparted by the fluidic jet. Thus, there was an overall increase in the yaw angle, ultimately resulting in a flow overturning at the casing at the overblown condition. At this condition, there was also a significant underturning of about 14° at span 0.7, which was on account of enhanced secondary flows.

The radial velocity for the flat wall case remained close to zero throughout the span. But it assumed slightly negative values for the baseline case. This was possibly because of the introduction of the leakage flow that was pushing the bulk flow away from the casing upon its re-entry. With the introduction of the fluidic jet, there was an increase in the re-entering mass flow. This was the reason for the slightly more negative radial velocities near the casing for all jet pressures. At the highest jet pressure, the radial velocity showed a very different pattern, which was due to the considerably enhanced secondary flows.

An interesting phenomenon was observed in these pitch-averaged results. As the jet pressure was raised, the fluidic jet case results showed a tendency to move from the baseline case towards the flat wall case. The closest match with the flat wall case was observed at the 1.1 jet pressure ratio. Since this jet pressure ratio was also seen to give the best performance in terms of leakage reduction (Figure 24) and the rotor exit loss (Figure 25), it might be considered to be the optimum among the jet pressure ratios tested in the present study. This was also a positive indication that the fluidic jet was taking the exit flow field from leakage conditions towards the ideal (no leakage) conditions.

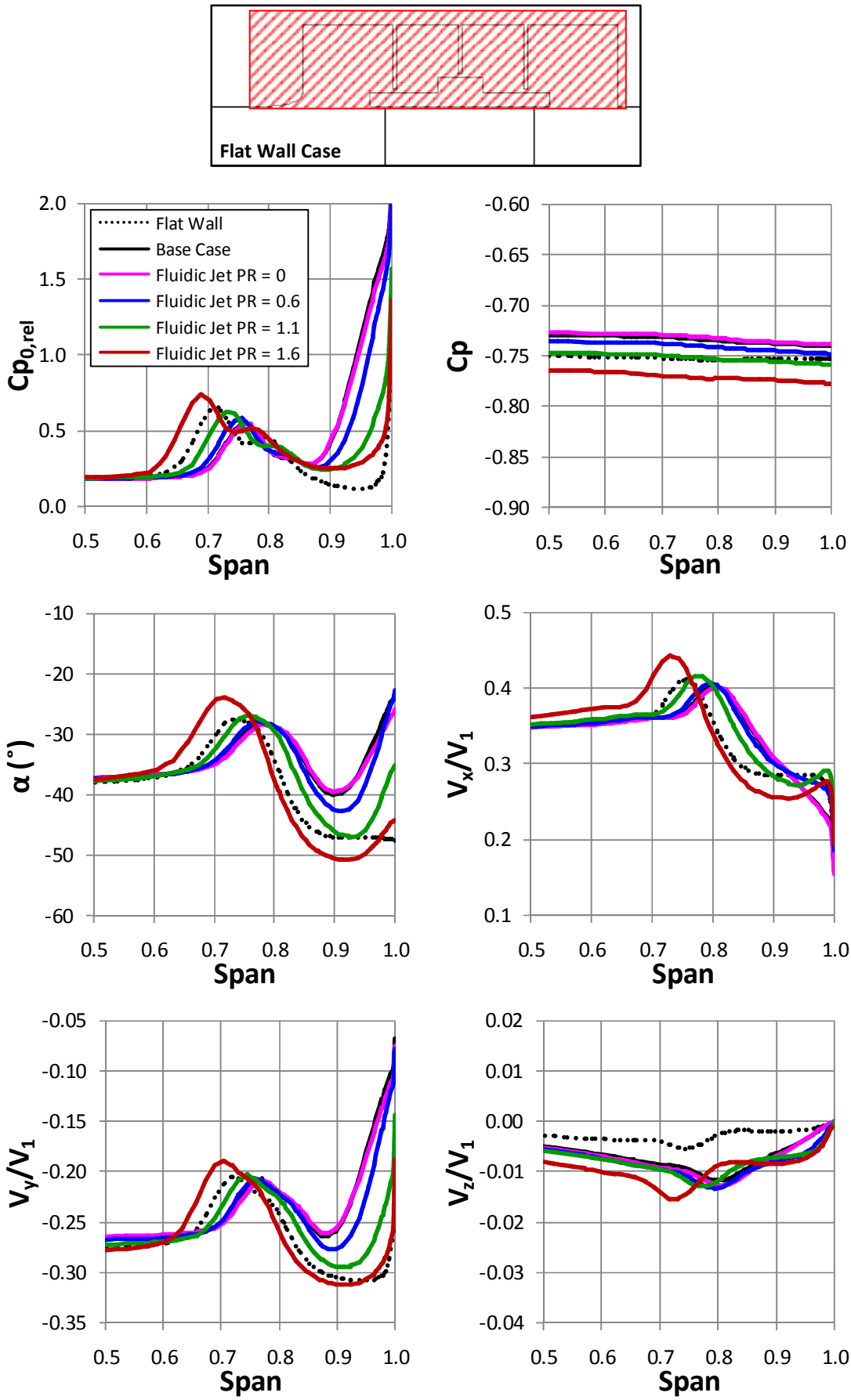

Figure 35, Pitch-averaged Results of Jet Pressure Ratio Comparison at 2.0C_x

7.3.2 Loss Breakdown

The impact of the fluidic jet on the loss distribution behind the rotor is discussed in this section. Denton [1] separated turbomachinery losses into three main categories:

- Tip leakage loss over the blade/shroud
- Profile or wake loss
- Endwall or secondary loss

He also equated, that generally, each of these categories made up for one-third of the total loss, i.e. the loss was equally divided between the three. So the purpose of this loss breakdown was to first determine these loss contributions for the baseline case. Then, it was to investigate how these individual contributions were affected by the introduction of the fluidic jet. For this, the percentage contribution from each category was calculated at the $2.0C_x$ location for the baseline case and then the fluidic jet case at different jet pressures. Since the present blade had a high aspect ratio (2:1) for cascade purposes, it would be expected to give a substantial profile loss contribution. So the loss breakdown was performed for half span (span 0.5 – 1).

The procedure used was as follows: The pitch-averaged relative total pressure loss coefficient (equation 5) at plane $2.0C_x$ contained all three identified types of loss ($\overline{Cp0_{L+P+E}}$). So the profile loss was subtracted from it to obtain the pitch-averaged leakage and endwall loss ($\overline{Cp0_{L+E}}$). As the plane $1.1C_x$ was located just behind the blade trailing edge, it only contained the profile and endwall losses. So the pitch-averaged loss at plane $1.1C_x$ was subtracted from that at plane $2.0C_x$. This left behind only the pitch-averaged leakage loss at plane $2.0C_x$ ($\overline{Cp0_L}$). Then these pitch-averaged losses were converted to mass-averaged values ($\overline{\overline{Cp0}}$) using the following expression for the present incompressible case:

$$\overline{\overline{Cp_0}} = \frac{\int_{span=0.5}^{span=1.0} \overline{Cp_0 . V_x} ds}{\int_{span=0.5}^{span=1.0} \overline{V_x} . ds} \tag{14}$$

The mass-averaged loss coefficients $\overline{\overline{Cp0_{L+P+E}}}$, $\overline{\overline{Cp0_{L+E}}}$ and $\overline{\overline{Cp0_L}}$ were directly calculated from the above expression. Others were obtained as follows:

$$\overline{\overline{Cp0_P}} = \overline{\overline{Cp0_{L+P+E}}} - \overline{\overline{Cp0_{L+E}}} \quad (15)$$

$$\overline{\overline{Cp0_E}} = \overline{\overline{Cp0_{L+E}}} - \overline{\overline{Cp0_L}} \quad (16)$$

Figure 36 shows the results from these calculations for all the cases. It may be noted that there were no hub side secondary flows in the present study. Had they been present, the endwall loss contribution could be expected to at least double. So, for the baseline case, the contributions from the leakage, profile and endwall losses would then become 27.5, 34.5 and 38 percent respectively. This would have been close to the 33/33/33 split proposed by Denton.

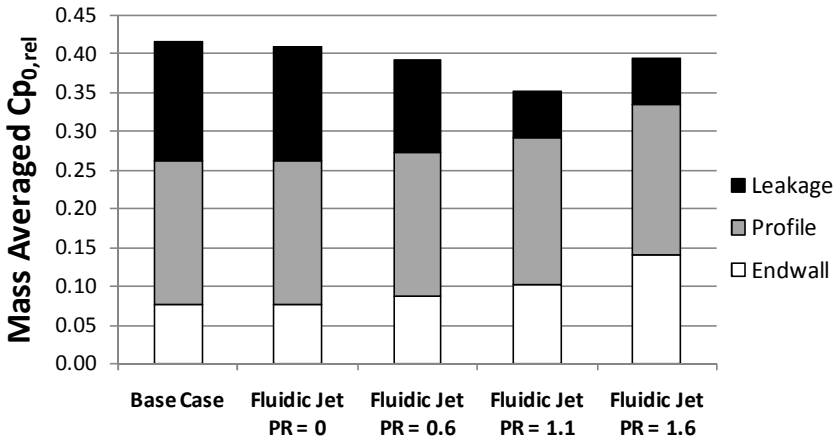

Figure 36, Loss Breakdown at 2.0C_x

The pitch-averaged loss coefficient in Figure 35 had shown the zero jet pressure case results to nearly superimpose on the baseline case results. So it was not surprising that at zero jet pressure, the loss contributions for the fluidic jet case were almost the same as the baseline case. However, for the zero jet pressure case, a 4 percent reduction was observed in the leakage contribution leading to a 1 percent reduction in the total loss. As the jet pressure was raised, the leakage contribution dropped, the endwall contribution increased and the profile contribution increased slightly. In fact, at the 1.1 jet pressure ratio, the leakage contribution was reduced by approximately 60 percent compared to the baseline case. As the increase in the endwall contribution was only about 30 percent, the total loss was reduced by more than 15 percent from the baseline case. It was interesting to note that, although the jet pressure was raised linearly, the reduction in the leakage contribution was not linear.

The highest drop was observed in going from 0.6 to 1.1 jet pressure ratio. Increasing the jet pressure ratio further to 1.6 did not reduce the leakage loss much. But the endwall contribution increased so significantly that it resulted in an overall loss increase.

7.3.3 Work and Flow Coefficients

The work coefficient (ψ) and the flow coefficient (ϕ) have a direct bearing on the efficiency of a turbine. The fluidic jet was seen to increase the mass flow through the rotor and the rotor work, and as a result, it modified these non-dimensional coefficients. So they were calculated for the baseline case and the different jet pressure ratios of the fluidic jet case. The coefficients were defined as:

$$\psi = \frac{V_{y1} - V_{y2}}{U} \tag{17}$$

$$\phi = \frac{V_{x1}}{U} \tag{18}$$

where V_{x1} is the mass averaged axial velocity at the rotor leading edge, V_{y1} is the mass averaged tangential velocity at the rotor leading edge, V_{y2} is the mass averaged tangential velocity at the rotor trailing edge and U is the blade velocity. As the jet pressure was raised, the mass flow and the turning through the rotor increased and so a rise in the work coefficient and the flow coefficient was observed. Such a behaviour of these coefficients should result in a reduction in the turbine efficiency. In order to determine the reduction that these increments would bring, the Smith's efficiency chart was consulted as shown in Figure 37.

Since the increments were very small, the baseline case and the fluidic jet cases were placed very close to each other on the chart. In fact, they could all be enclosed within the tiny red box drawn inside the chart. This suggested that the reduction in efficiency of the fluidic jet case due to changes in the work and flow coefficients would be negligible.

A zoom of the plot of work coefficient against the flow coefficient from the present results is also presented in Figure 37. It was observed that the coefficients were

within the usual range of high pressure turbines (ψ = 1.0 to 2.0; ϕ = 0.5 to 0.65). They matched quite closely for the baseline case and the zero jet pressure case. The slightly lower coefficients for the latter could be due to its 2 percent higher leakage mass flow. This would cause a small reduction in the flow through the rotor and hence the coefficients. It was also noticed that the rise in the coefficients was almost linear up to the jet pressure ratio of 1.1. At the overblown condition, although the turning through the rotor was reduced due to the enhanced secondary flows, this was outweighed by the extra work obtained from the jet fluid entering through the inlet cavity. So there was a net rise in the work coefficient.

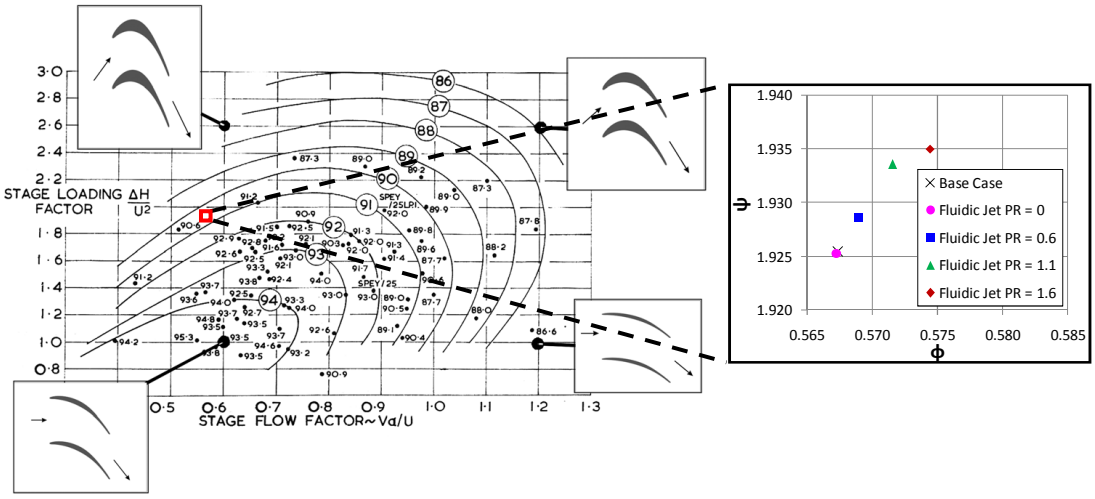

Figure 37, Smith Efficiency Chart as produced in Coull et al. [39]

8 Discussion

8.1.1 Fluidic Jet Performance

Fluidic jet use until now has been limited to reducing the leakage quantity in turbines. The study presented in this thesis showed fluidic jets to be promising in terms of leakage loss reduction too.

For the best performing operating jet pressure simulated, there was a leakage mass flow reduction of 77 percent which translated to a 1.1 percent increase in the rotor power output compared to the baseline case. At the same time, the leakage loss contribution was reduced by 60 percent. After taking into account the 30 percent increase in the secondary loss, this resulted in a 15 percent reduction in the total loss at the rotor exit. Furthermore, the rotor exit yaw angle was improved by almost 12° near the casing, so that it was only 3° away from its mid-span value. However, there was a 0.6 percent drop in the overall efficiency of the rotor. It was because the rise in the rotor work was outweighed by the energy supplied to the jet and the increased pressure drop across the rotor. It must be kept in mind that the present rotor blade profile gave a high absolute yaw angle of 36.2° at the exit. In many turbines, however, the flow exits the rotor almost in an axial direction. If the fluidic jet were to be used on such a rotor, the jet energy required to turn the re-entering flow would be smaller. This would also reduce the rotor pressure drop and the result would be a positive impact on the efficiency. Hence, the efficiency drop observed in the present study should not be taken as a general conclusion.

Another point to remember is that as the study was performed on a single rotor configuration, the impact on downstream rows was not taken into consideration. In a multi-stage turbine configuration, a fluidic jet implementation like the one in the present study would improve the downstream incidence. This would imply a reduction in the secondary loss of downstream rows. Lower secondary losses would mean less dissipation of the useful energy of the working fluid and ultimately, an increase in the turbine efficiency. The turning vanes used by Rosic et al. [29] raised the measured turbine efficiency by 0.4 percent by reducing the re-entry mixing and

downstream losses. The present study indicated that this could also be achieved through a fluidic jet, along with a simultaneous increase in the turbine work. So, the fluidic jet could result in an overall efficiency gain in a full turbine configuration. Its advantage over turning vanes would be that it would not hinder the axial movement of the rotor.

Due to the rotor axial movement, the distance between the fluidic jet and the upright tooth will vary during the turbine operation. This, in turn, will cause variations in the blockage effect of the fluidic jet. Thus, the performance of the fluidic jet may change depending on the axial position of the rotor.

8.1.2 Denton's Entropy Model

The fluidic jet success was based on Denton's equation [1] for entropy generation due to mixing in a shrouded turbine. This equation was based on a simple two dimensional model of leakage interaction. So it considered the re-entering flow rate and the differences in the axial and the tangential components of the mixing fluids as the only sources of entropy creation. In the present study, the axial velocity difference was found to be negligible for the baseline case. But there was a considerable difference in the tangential velocities. The fluidic jet was able to reduce the tangential velocity difference significantly. It did however increase the re-entering flow rate, but the maximum increase was only approximately 0.5 percent of the bulk flow. So overall, considering only the above entropy sources, one would expect the fluidic jet case to have lower entropy due to mixing than the baseline case.

However, this comparison was found not to be so straightforward in the present study. Like in most real turbines, there were more sources of entropy generation than those considered by the above equation. For example, as observed during the flow investigations, vortical structures were formed inside all of the cavities and there was the shroud trailing edge vortex which varied between cases. Since it was difficult to separate the entropy that was created only through the mixing between the re-entering flow and the bulk flow, a direct comparison with Denton's equation could not be performed.

The fluidic jet case showed much lower entropy generation rates due to re-entry mixing and under the seal teeth, but significant entropy was seen to be created downstream of the fluidic jet and within the re-entering wall jet. As a result, at the jet pressure ratio of 1.1, its mass-averaged entropy at the $2.0C_x$ plane was found to be approximately 5 percent higher compared to the baseline case. The high entropy layer behind the rotor was, however, thinner for the fluidic jet case. Figure 38 presents the entropy contours for the baseline case and the fluidic jet case at the 1.1 jet pressure ratio.

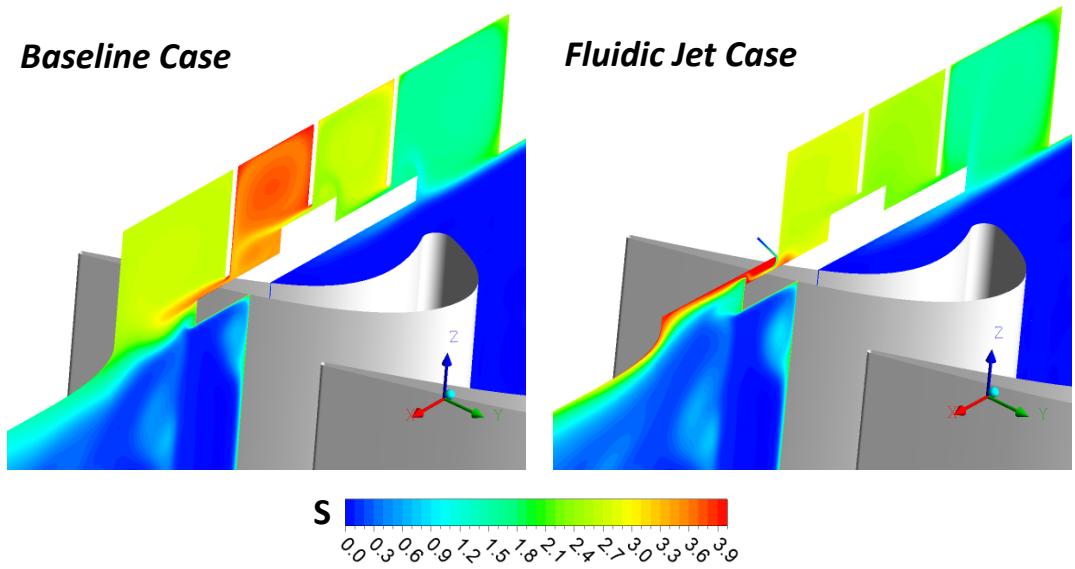

Figure 38, Fluidic Jet Impact: Entropy on Meridional Plane

It might seem counter-intuitive to have a higher entropy and a lower loss simultaneously as for the fluidic jet case. But the reason for this behaviour was that since the fluidic jet itself was supplied at a high energy, it was able to retain a significant amount of it even after all the entropy creation. This resulted in a high energy, or in other words, low loss fluid at the rotor exit.

8.1.3 Exit Cavity Depth

A major factor which helped configuration *Uth* to give the highest reduction in the re-entry mixing loss was the reduced depth of the exit cavity. Interestingly, Rosic et al. [8], in their computational investigations of a 1.5 stage turbine, had found that a reduced exit cavity enhanced the secondary flows in the downstream row. Similar

results were obtained experimentally by Schlienger et al. [26] who had used contoured inserts at the exit cavity. The reason for their findings was that the leakage flow re-entered the bulk flow in a very different direction and, due to the reduced cavity depth, propagated directly to the downstream row. In the present study however, the re-entering flow had been turned towards the bulk flow by the fluidic jet. So, although it formed a wall jet and might have continued directly towards a hypothetical downstream row, it would still have reduced its secondary flows.

The zero jet pressure case of configuration *Uth* was somewhat like the baseline case with a reduced exit cavity. The only difference was that, because of the last upright tooth, the re-entering flow formed a wall jet instead of the free jet found in the baseline case. When its loss coefficient was investigated at the 2.0W plane, the leakage loss was found to be 4 percent lower compared to the baseline case. As a result, there was a 1 percent reduction in the mass-averaged rotor exit loss coefficient. This agreed well with the results of Rosic et al. [8] who had shown that a smaller exit cavity depth reduced the in-cavity mixing and so improved the leakage - bulk flow interaction.

Hence, it may be understood that a reduced exit cavity certainly works better in a fluidic jet case designed to turn the re-entering flow. But if a fluidic jet is not used, the exit cavity depth is a trade-off between the in-cavity mixing and the downstream row losses, and should be selected with care.

8.1.4 Rotor Secondary Flows

The baseline case showed weaker secondary flows compared to the flat wall case. It was because of the removal of the incoming boundary layer by the inlet cavity. In fact, due to the rotor potential field, more fluid was pushed into the inlet cavity in front of the blade leading edge. This made the boundary layer even thinner in this region, helping further in the reduction of secondary flows.

For the fluidic jet case, the blocking of the leakage flow intensified the interaction between the inlet cavity fluid and the bulk flow. As more of the inlet cavity fluid was forced to re-enter the bulk flow, it increased the boundary layer skewness at the rotor

leading edge. Thus, an increase in the jet pressure caused an enhancement of the secondary flows in the rotor. This corresponded with the observations made by Rosic et al. [8] in their numerical study of clearance variation in a 1.5 stage turbine. A reduction in the seal clearance in their case, which had a similar effect as increasing the fluidic jet pressure, was seen to enhance the rotor secondary flows for the same reason. In the fluidic jet case, this could be dealt with by concepts such as non-axisymmetric endwall profiling [38].

To sum up, fluidic jets are a good idea for leakage loss reduction in shrouded turbines. They have the ability to simultaneously reduce the leakage quantity as well as the re-entry mixing loss. In addition, they also have the potential to improve the downstream row losses and bring overall efficiency gains in the turbine. Although the fluidic jet caused a drop in the efficiency of the rotor, the high rotor exit yaw angle and the non-inclusion of a downstream stator mean that the efficiency drop seen in the present study is not a general conclusion.

9 Conclusions

A series of CFD calculations were carried out to investigate the potential of fluidic jet barriers in reducing the leakage loss in shrouded turbines. The following conclusions emerged:

- The study demonstrated for the first time, the dual potential of fluidic jets in reducing the leakage flow and the re-entry mixing loss.
- At the best operating fluidic jet pressure ratio, the leakage quantity was reduced by 77 percent. This generated a 1.1 percent increase in the rotor work. At the same time, there was a 60 percent reduction in the leakage loss. This was due to: a) improved re-entry mixing, and b) reduced exit cavity depth.
- Due to the fluidic jet, there was a 12° improvement in the rotor exit yaw angle near the casing so that its difference from the mid-span value was only 3°. This should reduce the downstream row secondary loss and thus improve the stage efficiency.
- The fluidic jet enhanced the rotor secondary flows and hence increased the secondary loss by 30 percent. But due to the leakage loss reduction, the overall loss at the rotor exit was reduced by 15 percent. The effect on wake losses was negligible.
- There was a 0.6 percent drop in the overall efficiency of the rotor for the fluidic jet case. This was because the energy supplied to the jet and the increase in the pressure drop across the rotor outweighed the benefits of the fluidic jet.

10 Recommendations

- For configuration *Uth*, changing the distance between the fluidic jet and the tooth can improve the blockage further. This could be investigated. It would also give an indication of how the fluidic jet performance would be affected by the rotor axial movement during turbine operation.
- In this thesis, the fluidic jet was always supplied at the absolute rotor exit yaw angle. If this angle is increased, keeping the jet pressure constant, there is a higher turning of the re-entering flow but a lower blockage. So there is scope for optimization of this angle for each jet pressure.
- A downstream row could be computed to include downstream effects in the overall efficiency.
- The width of the fluidic jet used in the present study is likely to be less than 1mm in a real machine. This makes the manufacturing aspect of fluidic jet incorporation challenging. However, holes of such size are common in industrial turbines, such as those found in the blades for cooling purposes, combustion chambers and afterburners. Laser drilling is now an established practice for producing such holes [40]. The extensive use of turbines in the field of propulsion and power generation means that even small gains from the fluidic jet can recover the extra cost involved in the manufacturing. Finally, if the flow exits the rotor axially, then there is no need to impart a tangential momentum to the fluidic jet. This should simplify the manufacturing and thus reduce the manufacturing cost.

11 References

1. Denton, J.D., *The 1993 IGTI Scholar Lecture: Loss Mechanisms in Turbomachines.* Journal of Turbomachinery, 1993. **115**(4): p. 621-656.
2. Curtis, E., M., Denton, J., D., Longley, J., P., Rosic, B. *Controlling Tip Leakage Flow Over a Shrouded Turbine Rotor Using an Air-Curtain*. ASME Paper No. GT2009-59411.
3. Hogg, S., I., Ruiz, I., G. *Fluidic Jet Barriers for Sealing Applications*. ASME Paper No. GT2011-45353.
4. Auld, A., Hilfer, M., Hogg, S., Ingram, G., Messenger, A. *Application of an Air-Curtain Fluidic Jet Type Seal to Reduce Turbine Shroud Leakage*. ASME Paper No. GT2013-94198.
5. Yoon, S., Curtis, E., Denton, J., Longley, J. *The effect of clearance on shrouded and unshrouded turbines at two levels of reaction*. ASME Paper No. GT2010-22541.
6. Bindon, J., P., *The measurement and formation of tip clearance loss.* Journal of Turbomachinery, 1989. **111**(3): p. 257-263.
7. Takeshi, K., Matsuura, M., Aoki, S., Sato, T. *An experimental study of heat transfer and film cooling on low aspect ratio turbine nozzles*. ASME Paper No. 89-GT-187.
8. Rosic, B., Denton, J., D., Curtis, E., M., *The Influence of Shroud and Cavity Geometry on Turbine Performance: An Experimental and Computational Study-Part I: Shroud Geometry.* Journal of Turbomachinery, 2008. **130**(4).
9. Wolter, K., Giboni, A., Peters, P., Menter, J., R., Pfost, H. *Experimental and numerical investigation of the unsteady leakage flow through the rotor tip labyrinth of a 1.5-stage axial turbine*. ASME Paper No. GT2005-68156.
10. Pfau, A., Schlienger, J., Rusch, D., Kalfas, A., I., Abhari, R., S., *Unsteady flow interactions within the inlet cavity of a turbine rotor tip labyrinth seal.* Journal of Turbomachinery(Transactions of the ASME), 2005. **127**(4): p. 679-688.
11. Denton, J., D., Johnson, C., G. , *Tip Leakage Loss of Shrouded Turbine Blades.* CEGB report R/M/N848, 1976.
12. Gier, J., Stubert, B., Brouillet, B.,de Vito, L., *Interaction of Shroud Leakage Flow and Main Flow in a Three-Stage LP Turbine.* Journal of Turbomachinery, 2003. **127**(4): p. 649-658.
13. Peters, P., Breisig, V., Giboni, A., Lerner, C., Pfost, H., *The Influence of the Clearance of Shrouded Rotor Blades on the Development of the Flowfield and Losses in the Subsequent Stator.* ASME Paper No. 2000-GT-0478.
14. Adami, P., Milli, A., Martelli, F., Cecchi, S. *Comparison of different shroud configurations in high-pressure turbines using unsteady CFD*. ASME Paper No. GT2006-90442.
15. Hunter, S., D., Manwaring, S., R. *Endwall Cavity Flow Effects on Gaspath Aerodynamics in an Axial Flow Turbine: Part I—Experimental and Numerical Investigation*. ASME Paper No. 2000-GT-0513.
16. Pfau, A., Treiber, M., Sell, M., Gyarmathy, G., *Flow interaction from the exit cavity of an axial turbine blade row labyrinth seal.* Journal of Turbomachinery, 2001. **123**(2): p. 342-352.
17. Giboni, A., Wolter, K., Menter, J., R., Pfost, H. *Experimental and numerical investigation into the unsteady interaction of labyrinth seal leakage flow and main flow in a 1.5-stage axial turbine*. ASME Paper No. GT2004-53024.
18. Giboni, A., Menter, J., R., Peters, P., Wolter, K., Pfost, H., Breisig, V. *Interaction of labyrinth seal leakage flow and main flow in an axial turbine*. ASME Paper No. GT2003-38722.

19. Peters, P., Menter, J., R., Pfost, H., Giboni, A., Wolter, K. *Unsteady Interaction of Labyrinth Seal Leakage Flow and Downstream Stator Flow in a Shrouded 1.5 Stage Axial Turbine*. ASME Paper No. GT2005-68065.
20. Rosic, B., Denton, J., D., Pullan, G., *The Importance of Shroud Leakage Modeling in Multistage Turbine Flow Calculations.* Journal of Turbomachinery, 2005. **128**(4): p. 699-707.
21. Cherry, D., Wadia, A., Beacock, R., Subramanian, M., Vitt, P. *Analytical investigation of a low pressure turbine with and without flowpath endwall gaps, seals and clearance features*. ASME Paper No. GT2005-68492.
22. Wallis, A., M., Denton, J., D., Demargne, A., A., J., *The Control of Shroud Leakage Flows to Reduce Aerodynamic Losses in a Low Aspect Ratio, Shrouded Axial Flow Turbine.* Journal of Turbomachinery, 2000. **123**(2): p. 334-341.
23. Casey, M., V., Pfost, H., Wolter, K., Anker, J., E., *Deckbandströmungseinfluss III, Abschlussbericht des FVV-Vorhabens Nr. 801.* FVV-Heft R. **527**.
24. Xiao, Y., Amano, R., S., *Leakage flow over shrouded turbine blades.* ASME Paper No. 2000-GT-0193.
25. Xiao, Y., Amano, R., S. *Study of losses in a leakage flow through the passage of shrouded turbine blades with swirl velocity*. ASME Paper No. 2001-GT-0121.
26. Schlienger, J., Pfau, A., Kalfas, A., I., Abhari, R., S. *Effects of labyrinth seal variation on multistage axial turbine flow*. ASME Paper No. GT2003-38270.
27. Pfau, A., Kalfas, A., I., Abhari, R., S., *Making use of labyrinth interaction flow.* TRANSACTIONS-AMERICAN SOCIETY OF MECHANICAL ENGINEERS JOURNAL OF TURBOMACHINERY, 2007. **129**(1): p. 164.
28. Rosic, B., Denton, J., D., Curtis, E., M., Peterson, A., T., *The Influence of Shroud and Cavity Geometry on Turbine Performance: An Experimental and Computational Study-Part II: Exit Cavity Geometry.* Journal of Turbomachinery, 2008. **130**(4).
29. Rosic, B., Denton, J., D., *Control of shroud leakage loss by reducing circumferential mixing.* Journal of Turbomachinery, 2008. **130**(2): p. 021010.
30. Gao, J., Zheng, Q., Yue, G., Sun, L., *Control of shroud leakage flows to reduce mixing losses in a shrouded axial turbine.* Proceedings of the Institution of Mechanical Engineers, Part C: Journal of Mechanical Engineering Science, 2011.
31. Messenger, A., *Design of a Fluidic Seal Test Facility*. 2013, Durham University M. Eng Research Project
32. Shapiro, A., H., *The Dynamics and Thermodynamics of Compressible Fluid Flow*. 1953, New York: Wiley.
33. Denton, J., D. *Some limitations of turbomachinery CFD*. ASME Paper No. GT2010-22540.
34. Bagshaw, D., A., Gregory-Smith, D., G., Ingram, G., L., Stokes, M., R. *A turbine cascade facility for secondary flow research*. ASME Paper No. GT2006-90868.
35. Moore, H., Gregory-Smith, D. *Transition effects on secondary flows in a turbine cascade*. ASME Paper No. 96-GT-100.
36. Herwig, H., Kock, F., *Direct and indirect methods of calculating entropy generation rates in turbulent convective heat transfer problems.* Heat and mass transfer, 2007. **43**(3): p. 207-215.
37. Moffatt, H., K., *The degree of knottedness of tangled vortex lines.* Journal of Fluid Mechanics, 1969. **35**(01): p. 117-129.
38. Ingram, G., L., *Endwall profiling for the reduction of secondary flow in turbines*. 2003, Durham University PhD Thesis.
39. Coull, J., D., Hodson, H., P., *Blade Loading and Its Application in the Mean-Line Design of Low Pressure Turbines.* Journal of Turbomachinery, 2013. **135**(2): p. 021032.

40. Naeem, M., Lane, C., Valley, S, *Advancement in laser drilling for aerospace gas turbines.* Proceedings of PICALEO, 2008: p. 197-202.